

# A Review of Experimental and Computational Advances in Thermal Boundary Conductance and Nanoscale Thermal Transport across Solid Interfaces

Ashutosh Giri and Patrick E. Hopkins\*

Interfacial thermal resistance is the primary impediment to heat flow in materials and devices as characteristic lengths become comparable to the mean-free paths of the energy carriers. This thermal boundary conductance across solid interfaces at the nanoscale can affect a plethora of applications. The recent experimental and computational advances that have led to significant atomistic insights into the nanoscopic thermal transport mechanisms at interfaces between various types of materials are summarized. The authors focus on discussions of works that have pushed the limits to interfacial heat transfer and drastically increased the understanding of thermal boundary conductance on the atomic and nanometer scales near solid/solid interfaces. Specifically, the role of localized interfacial modes on the energy conversion processes occurring at interfaces is emphasized in this review. The authors also focus on experiments and computational works that have challenged the traditionally used phonon gas models in interpreting the physical mechanisms driving interfacial energy transport. Finally, the authors discuss the future directions and avenues of research that can further the knowledge of heat transfer across systems with broken symmetries.

leads to large bottlenecks to heat transfer, and ultimately dictate device functionality, reliability, and failure thresholds.<sup>[1–9]</sup>

The efficacy of heat transfer across heterogeneous material interfaces is quantified by the thermal boundary conductance,  $h_K$ , which relates the heat flux to the temperature drop at the interface. Mathematically, the thermal boundary conductance is inversely related to the thermal boundary resistance,  $R_K$ , and is related to the temperature drop across the interfacial region via  $h_K = \frac{1}{R_K} = Q/\Delta T$ , where  $Q$  is the power flux across the interfacial region (with units of  $\text{W m}^{-2}$ ),  $\Delta T$  is the temperature drop (with units of K), and the units of  $h_K$  are in  $\text{W m}^{-2} \text{K}^{-1}$  (with its inverse of  $R_K$  in units of  $\text{m}^2 \text{K W}^{-1}$ ). This thermal boundary conductance has become a critical thermal property that dictates the ability to dissipate or confine energy more efficiently in a wide range of applications and technologies as depicted in

## 1. Introduction

The rapid miniaturization of device dimensions has led to mean-free paths of energy carriers approaching or even surpassing typical length scales in homogeneous materials. In devices that contain a high density of material interfaces, reduced dimensionalities to increase operating frequencies, or high localized power densities, thermal transport across interfaces ultimately dictates the overall thermal resistance that


Figure 1 showing the current technologies reliant on nanoscale thermal transport across interfaces for their efficient usage. For example, on the one hand, high thermal conductances and low thermal resistances associated with heterogeneous material interfaces ensure appropriate operating temperatures and power dissipation out of active regions in electronic devices (e.g., high power transistors, high frequency photodiodes, light emitting diodes, computing architectures, and phase change memory).<sup>[1–9]</sup> On the other hand, low interfacial conductances can also lead to ultralow thermal conductivities in materials such as nanolaminates and superlattices that are desirable for applications reliant on thermal confinement and large temperature gradients, such as thermal barrier coatings, thermoelectric materials, photothermal medical therapies, and phase change memory.<sup>[10–15]</sup> Therefore, to fully realize the potential and proper functionality of these applications and technologies, the complete understanding of thermal boundary conductance becomes imperative.

The first quantitative measurements of  $h_K$  were conducted by Kapitza in 1941 between solid Cu and liquid He. As such, “thermal boundary conductance” is often interchanged with “Kapitza conductance” in literature.<sup>[16]</sup> We note that the term Kapitza conductance technically refers to the conductance across an infinitesimally thin (atomically perfect and abrupt) surface or interface. However, thermal boundary conductance

Dr. A. Giri, Prof. P. E. Hopkins  
Department of Mechanical and Aerospace Engineering  
University of Virginia  
Charlottesville, VA 22904, USA  
E-mail: phopkins@virginia.edu

Prof. P. E. Hopkins  
Department of Materials Science and Engineering  
University of Virginia  
Charlottesville, VA 22904, USA

Prof. P. E. Hopkins  
Department of Physics  
University of Virginia  
Charlottesville, VA 22904, USA

 The ORCID identification number(s) for the author(s) of this article can be found under <https://doi.org/10.1002/adfm.201903857>.

DOI: 10.1002/adfm.201903857

can refer to a more general, spatially broad interfacial region. In this current review, we maintain the term thermal boundary conductance as nearly all the heat transport processes that we describe are occurring across interfacial regions, where phonon scattering a few atomic layers away from the actual “interface” can dictate the reported  $h_K$ . In fact, since the seminal work by Kapitza, tremendous progress has been achieved in understanding the interplay between interfacial properties and thermal boundary conductance, much of which involves the influence of the near-interface material properties and processes. The main factors that control  $h_K$  for solid/solid interfaces are i) the respective dispersion and density of states (DOS) for energy carriers in the two materials and the region near the interface, ii) the quality of the interface (for example, consider an “imperfect” interface with atomic mixing and roughness that can alter the vibrational properties of the solid as depicted in Figure 2a) along with the strength of interatomic interactions at the interface, and iii) temperature. These factors will be discussed in more detail throughout this review as we consolidate the recent experimental and theoretical advances that have drastically improved our understanding of interfacial transport. For example, we will discuss the recent interest in the existence of interfacial modes between two solids that are not present in the bulk of the materials (as depicted in Figure 2a) and their effect on enhancing interfacial heat transport. Moreover, a “perfect” interface in realistic situations is almost never realized, therefore, we will emphasize the effect of disorder and non-idealities and their effects on these interfacial modes that can potentially be used to effectively control electron and phonon scattering mechanisms occurring at and near interfaces.

For typical interfaces between crystalline solids that are dominated by vibrational heat conduction, typical values of  $h_K$  are in the range of 20 to 300 MW m<sup>-2</sup> K<sup>-1</sup> as shown in Figure 2b where we plot the experimentally measured values of  $h_K$  across various interfaces that have been measured over the past 30 years as a function of the ratio of elastic moduli between the two constituents. A better match between the elastic moduli of the crystalline materials is indicative of a better overlap in the vibrational DOS of the materials, which along with a high quality of interface, usually results in higher values of  $h_K$ . For example, it has been shown that by controlling the surface conditions between two silicon membranes that are mechanically joined via van der Waals (vdW) interactions,  $h_K$  can be varied by as much as 300%.<sup>[29]</sup> Likewise, epitaxial interfaces formed between well lattice matched materials such as SrRuO<sub>3</sub>/SrTiO<sub>3</sub> and TiN/MgO interfaces have demonstrated some of the highest measured values of phonon dominated  $h_K > 700$  MW m<sup>-2</sup> K<sup>-1</sup>.<sup>[24,25]</sup> Whereas, extremely low conductances are observed for interfaces formed between materials with highly dissimilar vibrational spectra (and a comparatively low ratio of elastic modulus) such as for bismuth deposited on a diamond substrate with  $h_K \approx 8.5$  MW m<sup>-2</sup> K<sup>-1</sup>, which represents one of the lowest ever measured conductances across solid interfaces at room temperature.<sup>[34]</sup> For comparison, the resistance that is posed by a single interface between these types of highly dissimilar materials can be as resistive as a 10–100 nm thick amorphous glass.

Recent advancements in experimental metrologies and computational tools have shown that interfaces formed with



**Ashutosh Giri** received his B.S. degree in Physics from Adelphi University in 2010 and his M.S. degree in Mechanical Engineering from University of Pittsburgh in 2012. In 2016, he received his Ph.D. from University of Virginia. He is currently a senior scientist at University of Virginia in Professor Patrick E. Hopkins group

focusing on experimental and computational studies of electron and phonon thermal transport and coupling across interfaces, thin films, and hybrid material systems.



**Patrick E. Hopkins** is a professor in the Department of Mechanical and Aerospace Engineering at the University of Virginia. Prior to his faculty appointment, he was a Harry S. Truman Fellow at Sandia National Labs immediately after he received his Ph.D. from the University of Virginia. Patrick's research interests are in measurements and simulations of thermal transport and

energy conversion in solid, liquids, gasses, and plasmas, with emphasis on quantifying and understanding the time and length scales of the energy carriers.

an amorphous solid can have very high conductances, which seems counterintuitive since disorder usually accompanies low conductances. The resistance associated with amorphous interfaces can defy the general trends that one would expect from interfaces formed between crystalline solids as discussed in the previous paragraph. This is shown in Figure 2b (square symbols) for several interfaces formed with amorphous materials that possess conductances that are much higher than the typical values observed for interfaces between crystalline solids.<sup>[17,18,35]</sup> Similarly, for material systems in which electrons dominate interfacial heat flow such as for metal/metal interfaces, the values of  $h_K$  can be greater than an order of magnitude as compared to the typical phonon-dominated conductances.<sup>[36–38]</sup> Electron-dominated scattering processes at interfaces occur much faster (with time scales in the single to 10's of picoseconds for metal/metal interfaces, depending on the metal film thicknesses relative to the electron mean-free paths) than the phonon-dominated scattering processes across interfaces, which take place in the several hundred picoseconds to nanosecond time scales. These key insights and advancements in the understanding of interfacial heat flow will be discussed in this review.

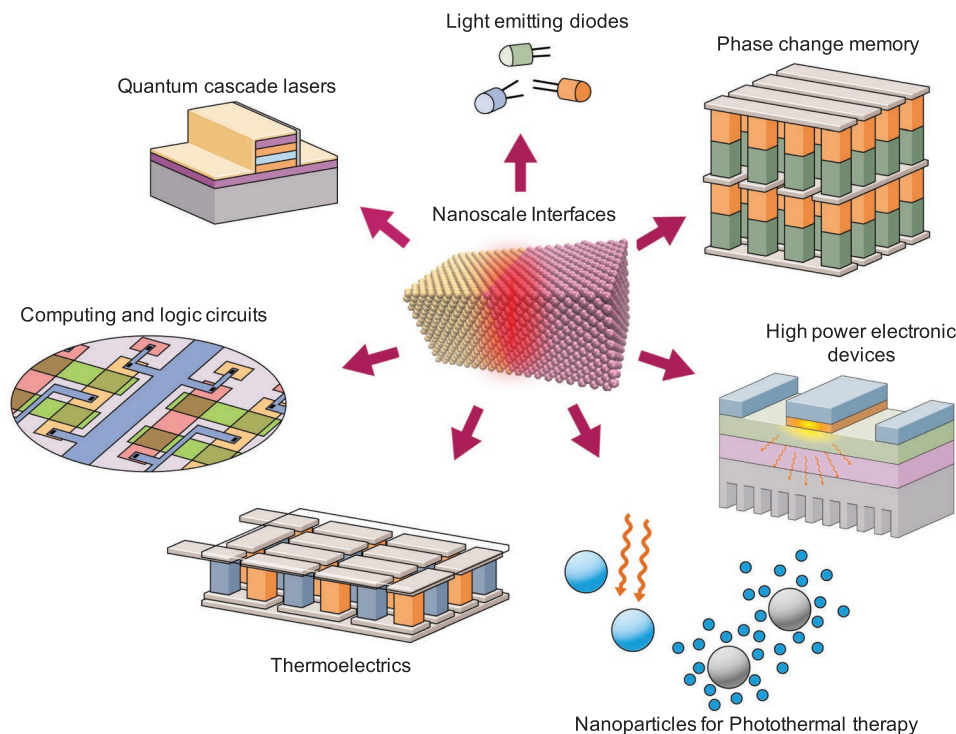


**Figure 1.** Illustration of various technologies reliant on dissipating or confining energy more efficiently through engineering nanoscale interfaces.

Several prior reviews have also highlighted some of the important advancements made in the understanding of Kapitza conductance at the nanoscale. The seminal article by Swartz and Pohl published in 1989 summarized the measurements conducted at cryogenic temperatures and presented the physical insights in terms of the acoustic mismatch model (AMM) and the diffuse mismatch model (DMM) and the phonon radiation limit that are still being used to interpret experimental results and provide key insights into the physical mechanisms dictating  $h_K$ . More recently, Hopkins<sup>[39]</sup> has summarized various experimental factors and near-interfacial defects and imperfections that drive  $h_K$ , mainly focusing on metal/nonmetal interfaces that are ubiquitous in time domain thermoreflectance (TDTR) and frequency domain thermoreflectance (FDTR) experiments. Monachon et al.<sup>[40]</sup> presented the materials perspective on  $h_K$  and reviewed various experimental techniques used to measure  $h_K$  from the past 30 years.

In this current review, we discuss the significant advances in understanding thermal boundary conductance both from experimental and computational fronts. We present the flaws that accompany the basic assumptions driving the theoretical models used extensively in literature to understand experimental results for  $h_K$  across various types of interfaces. Specifically, we highlight experiments and computational works that have challenged the use of the phonon gas models such as the DMM and AMM in interpreting the physical mechanisms driving interfacial energy transport. We start with the conceptual foundations that have shaped the conventional knowledge of interfacial conductance at the nanoscale. Then we present experimental works that have challenged these conventional theories and follow this with recent computational works that

have provided a deeper understanding of thermal boundary conductance and support the experimental findings. Then we present some of the recent advancements in understanding and controlling  $h_K$  across various material systems with different types of energy carriers. Finally, we present the main conclusions and provide an outlook for future research directions.

## 2. Commonly Invoked Semiclassical Formalisms for Predicting Thermal Boundary Conductance

A mathematical representation of heat flux across an interface from side 1 to side 2, in the most general form, is traditionally given in terms of the Landauer formalism as<sup>[41,42]</sup>

$$q_z^{1 \rightarrow 2} = \frac{1}{(2\pi)^3} \sum_j \int_0^{\pi/2} \int_0^{2\pi} \int_{k_{x,1}} \int_{k_{y,1}} \int_{k_{z,1} > 0} E_1 \tilde{v}_{j,1} \cos \theta_1 \sin \theta_1 f_{\zeta^{1 \rightarrow 2}}^{1 \rightarrow 2} d\tilde{k}_x d\tilde{k}_y d\tilde{k}_z d\theta_1 d\phi_1 \quad (1)$$

where the transport is in the  $z$ -direction perpendicular to the interface,  $j$  is the polarization,  $\theta_1$  and  $\phi_1$  are the azimuthal and elevation angles of the heat flux,  $\tilde{k}$  is the wave-vector (where  $x$ ,  $y$ , and  $z$  subscripts indicate individual Cartesian directions of this vector),  $E$  is the energy,  $\zeta^{1 \rightarrow 2}$  is the transmission coefficient from side 1 to 2,  $f$  is the distribution function for the energy carrier, and  $\tilde{v}_j$  is the carrier group velocity. Solving the full Equation (1) to calculate interfacial flux requires knowledge of spectral contributions from the energy carriers. Furthermore, due to the fact that thermal transport occurs when the system is driven out of equilibrium, it is technically incorrect to assume that the energy distribution can be approximated with an equilibrium distribution function such as the Fermi–Dirac



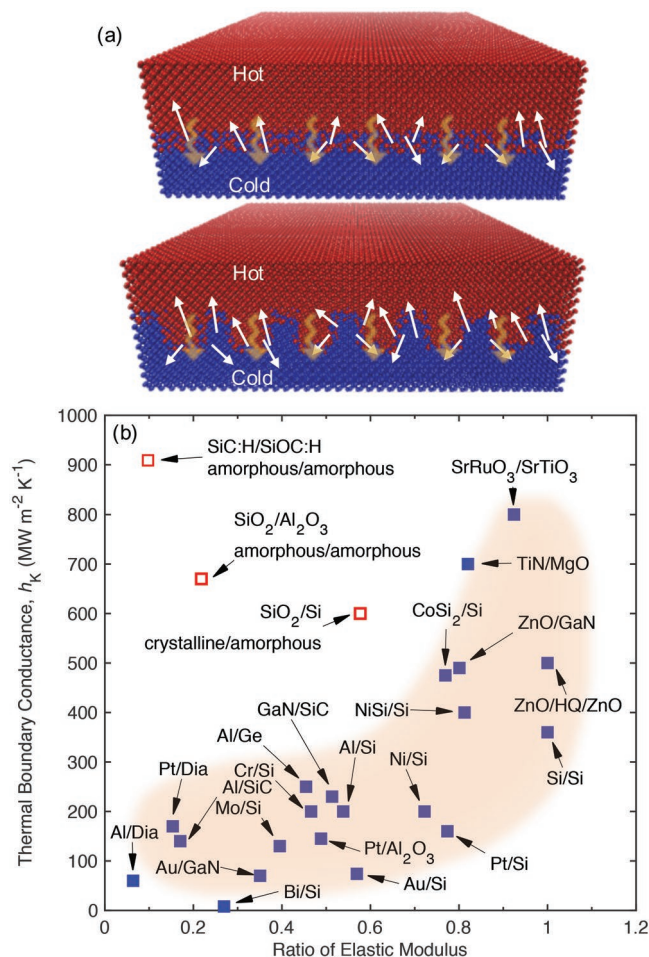


**Figure 2.** a) Schematic of atomically imperfect interfaces with atomic mixing and roughness between two solids in intimate contact. The arrows indicate interfacial modes localized near the interface that are not present in the bulk of either material. These interfacial modes can significantly enhance thermal boundary conductance. b) Experimentally measured thermal boundary conductance versus ratio of the elastic moduli of the two constituent materials (Si/SiO<sub>2</sub>,<sup>[17]</sup> SiO<sub>2</sub>/Al<sub>2</sub>O<sub>3</sub>,<sup>[18]</sup> Al/Diamond, Pt/Diamond,<sup>[19]</sup> Al/SiC,<sup>[20]</sup> Au/GaN,<sup>[21]</sup> Al/Ge,<sup>[22]</sup> GaN/SiC,<sup>[23]</sup> TiN/MgO,<sup>[24]</sup> SRO/STO,<sup>[25]</sup> Pt/Al<sub>2</sub>O<sub>3</sub>,<sup>[26]</sup> ZnO/GaN,<sup>[27]</sup> ZnO/HQ/ZnO,<sup>[28]</sup> Si/vdW (van der Waals interface)/Si,<sup>[29]</sup> Bi/Si,<sup>[30]</sup> Mo/Si, Al/Si, Ni/Si,<sup>[31]</sup> Cr/Si, Pt/Si, Au/Si,<sup>[32]</sup> NiSi/Si and CoSi<sub>2</sub>/Si<sup>[33]</sup>).

or Bose–Einstein distributions. In this context, the full Boltzmann transport equation needs to be solved to formulate  $f$ .<sup>[43]</sup> To reduce the computational cost and complexity, simplified statistical distribution functions are used and general assumptions regarding interfacial scattering are invoked to effectively predict the flux across interfaces between two materials. For example, the phonon flux impinging on an interface between two isotropic solids can be approximated under the isotropic assumption as

$$q = \frac{1}{8\pi^3} \sum_j \int_{\tilde{k}} \hbar \omega(\tilde{k}) D(\tilde{k}) f_0(\tilde{k}, T) \tilde{v}_{g,j}(\tilde{k}) d\tilde{k} \quad (2)$$

where  $f_0$  is described by the equilibrium Bose–Einstein distribution function,  $f_0 = 1/(e^{\frac{\hbar \omega}{k_B T}} - 1)$ , where  $k_B$  is the Boltzmann

constant,  $\hbar \omega$  is the energy of the phonon mode,  $\tilde{v}_{g,j}$  is the group velocity, and  $D(\tilde{k})$  is the density of states. The temperature derivative of Equation (2) with the inclusion of a transmission coefficient allows for the calculation of thermal boundary conductance, which is given as

$$h_K = \frac{1}{8\pi^3} \sum_j \int_{\tilde{k}} \hbar \omega(\tilde{k}) D(\tilde{k}) \frac{\partial f_0(\tilde{k}, T)}{\partial T} \tilde{v}_{g,j}(\tilde{k}) \zeta(\tilde{k})^{1 \rightarrow 2} d\tilde{k} \quad (3)$$

The transmission coefficient from side 1 to 2,  $\zeta(\tilde{k})^{1 \rightarrow 2}$ , can be approximated via various phonon–phonon scattering models such as the DMM and AMM.<sup>[44–46]</sup> In these models, the mismatch in acoustic properties or vibrational DOS, limits the interfacial phonon transmission, and therefore restricts the phonon flux that transmits across the interface. These models and further refinements of these models have been extensively described in the literature.<sup>[42,47–53]</sup>

The AMM was first formulated by Little in 1959 by solving the continuum elasticity equations.<sup>[45]</sup> This formulation is rooted in the assumptions that phonons perceive the interface as a specular boundary and specular wave interactions and transmission at the interface dictates the transport. Analogous to the mismatch in the refractive indices between two media in optics, the resistance at the interface between two solids under the AMM is due to the difference in the sound speeds that result from the acoustic impedances. Therefore, the transmission coefficient for phonon energy in side 1 to side 2 is given as

$$\zeta^{1 \rightarrow 2} = \frac{4\rho_1 c_1 \rho_2 c_2}{(\rho_1 c_1 + \rho_2 c_2)^2} \quad (4)$$

where  $\rho$  and  $c$  are the mass density and speed of sound, respectively. In this model, there are no atomistic properties intrinsic to the interface. It has been shown to successfully reproduce some measurements of  $h_K$  at cryogenic temperatures; however, at elevated temperatures above  $\approx 30$  K, the assumption of specular transmission is assumed to breakdown even for perfect interfaces.<sup>[24]</sup> For interfaces with imperfections and disorder, the AMM can no longer predict  $h_K$  even for temperatures as low as 1 K and a more suitable approach is the DMM.<sup>[44]</sup>

The basic assumption built in the DMM is that phonons are scattered diffusively at an interface, and thus they lose memory of their initial direction and polarization in the incident material. Further, an additional commonly invoked assumption is the elastic two-phonon scattering, where a phonon of frequency  $\omega$  in one side of the interface can only transmit energy across the interface to another phonon with the same frequency. This implies that the temperature dependence of  $h_K$  is dictated by the phonon population of the material with the lower Debye temperature (lower maximum frequency) between the two solids. Therefore, above the Debye temperature of the lower Debye temperature material, in the elastic scattering limit,  $h_K$  will be constant. There has been some success using the DMM to predict experimental measurements of  $h_K$  for various types of interfaces;<sup>[39]</sup> however, this agreement between theory and experiments can be considered a mere coincidence due to the fact that the crude assumptions made in the DMM render

the physical picture of the scattering mechanisms occurring at and near the interface to be incomplete, as we point out in detail below. As an example, previous works by Hopkins have developed extensions of the DMM to move beyond the elastic two-phonon scattering assumptions, and account for energy transmission among three or more phonons at an interface.<sup>[42,49,53–55]</sup> However, these formulations for inelastic scattering mechanisms in the DMM only account for energy conservation among multiple phonon energies, and do not account for the more constraining wave vector conservation and selection rules, mode-specific conversion probabilities, or more localized vibrational states (e.g., defects) which are well known to impact phonon scattering and transport in homogeneous solids. Moreover, both DMM and AMM do not take into account the atomistic nature at the interface, which is also one of the main flaws of these frameworks.

To assess upper limits to thermal conductance across interfaces, it is a common practice to replace  $\zeta$  with unity in Equation (3).<sup>[25,27,28]</sup> By doing so, it is effectively assumed that all thermally excited vibrational modes have a 100% probability of transmittance from side 1 to 2 of the imaginary interface in a crystal. Thus, the conductance is only limited by the thermal flux impinging on a crystallographic plane in a material. This sets an upper limit to thermal conductance and is the theoretical maximum conductance achievable in a material, a concept that will be used to interpret and analyze some of the experimental data presented in the later sections.

### 3. Failure of the Phonon Gas Models to Predict Thermal Boundary Conductance

The phonon gas model has been used to understand energy transfer mechanisms in crystalline materials with a well-defined periodicity, where the normal modes are obtained by solving the equations of motion of atoms in the harmonic limit. The modes appear as plane waves that combine to form wave packets that traverse with a group velocity defined by the dispersion of the crystal.<sup>[56]</sup> In this phonon gas model picture for materials with interfaces and broken symmetries, the scattering of these wave packets at the interface dictates the transmission probability of the normal modes. In other words, in the picture of the phonon gas model applied to thermal boundary conductance, phonons impinge at an interface and have certain probabilities of transmitting or reflecting depending on their transmission coefficients. However, the fundamental character and nature of the normal modes that would have existed separately in the two adjoined materials are changed due to the presence of an interface.<sup>[57–59]</sup> Therefore, phonon gas models such as the AMM and DMM, or even atomistic approaches that treat mode level thermal boundary conductance as a transmission problem similar to the Landauer theory, cannot properly account for the local vibrational interactions near the interface that are shown to influence the interfacial heat flow and thermal boundary conductance, as will be reviewed in Section 5.<sup>[57,60,61]</sup> Consequently, even though the phonon gas models may provide good agreement between theory and experiment, these models cannot provide a comprehensive insight into the experimental results and the vibrational interactions and conversions

near the interface that drive a significant portion of the thermal boundary conductance.

An approach to experimentally demonstrate the failure of the phonon gas model-based DMM to properly account for the spectral contribution of specific modes to  $h_K$  was developed by Hua et al.<sup>[43]</sup> In this work, Hua et al.<sup>[43]</sup> were able to extract the transmission coefficients for an Al/Si interface from TDTR data by replacing the macroscopic transfer function based on Fourier's law with a microscopic transfer function based on ab initio phonon transport theory. This is a unique way to analyze TDTR data since all of the other works that analyze TDTR data have so far only reported a spectrally averaged  $h_K$ , which does not shed light into the microscopic dynamics dictating heat flow across interfaces.

Figure 3 shows the spectrally resolved interfacial heat flux extracted from the experimental data, reported by Hua et al.<sup>[43]</sup> Their results show that the spectral contributions of modes below 4 THz are substantially more as compared to the predictions of the DMM owing to the higher transmission coefficient of these modes that cannot be captured by DMM. Their results show that the DMM cannot capture the importance of long wavelength contribution to  $h_K$ . Furthermore, their results suggest that the agreement between the mode averaged predictions of  $h_K$  from the DMM and the experimental results on various metal/nonmetal interfaces is mostly coincidental due to the under-prediction of contributions from low frequency modes and over-prediction of contributions from high frequency modes, which leads to error cancelation and agreement between theory and experiments.<sup>[31,33,62,63]</sup> This is clearly shown in the inset of Figure 3 where we plot the normalized interfacial heat flux from Hua et al.'s<sup>[43]</sup> ab initio approach and the DMM approach; the DMM is unable to capture the low frequency contributions while over-predicting the contributions from higher frequency modes. Furthermore, their measurements also show

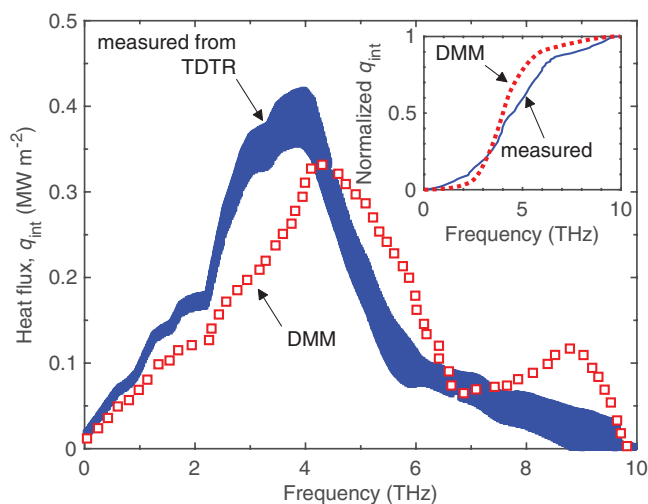


**Figure 3.** Spectral heat flux for Al/Si measured using time-domain thermoreflectance and ab initio based approach adapted from Hua et al.<sup>[43]</sup> Also shown are the calculations based on the diffuse mismatch model (red squares) that drastically under-predict the contributions from low frequency phonons (<4 THz). (Inset) Normalized spectral heat flux accumulations predicted by the diffuse mismatch model (dashed line) and the measurements from the ab initio based approach.

that phonons that have wavelengths shorter than the roughness at the interface are mostly reflected while phonons with longer wavelengths in comparison to the interface roughness are more likely to be transmitted. This experimentally derived phonon-interfacial roughness relationship provided experimental insight into previous theories of how phonons at interfaces and thermal boundary conductance are impacted by interfacial disorder and roughness.<sup>[64–68]</sup> This relationship between the spectral thermal boundary conductance and interfacial disorder provides an opportunity for selective phonon filtering across interfaces, since knowing the contributions of specific frequencies can enable the design of features at the interface that can target the contributions of certain groups of phonons in efficiently conducting heat across interfaces.

To correctly examine the validity of theoretical models on phonon-dominated thermal boundary conductance, it is imperative that these models be compared directly to experimental data on interfaces formed between high crystalline quality nonmetallic solids. Several studies have compared the various theoretical models to experimental results on metal/nonmetal interfaces;<sup>[25,31,32,39,40,69]</sup> however, as we point out later, the effect of electron–phonon coupling across the interface can lead to added complexities for theoretical models. Although noted by several works that this direct pathway for interfacial energy exchange does not exist for metal/nonmetal interfaces,<sup>[34,70,71]</sup> it has yet to be rigorously verified as we discuss further in Section 10. Therefore, we now discuss the direct comparison of experimental data on nonmetallic interfaces formed between ZnO and GaN with theoretical calculations rooted on DMM and atomic Green's function (AGF) to carefully access their validity, described in more detail by Gaskins et al.<sup>[27]</sup> While the previously described work by Hua et al.<sup>[43]</sup> demonstrated pitfalls in the phonon gas model-based DMM, this work by Gaskins et al.<sup>[27]</sup> on ZnO/GaN heteroepitaxial interfaces assessed the validity of the assumptions in the Landauer/transmission formalism-based AGF, in addition to the further invalidating assumptions of the DMM at this interface.

**Figure 4** shows  $h_K$  measured by TDTR across isolated heteroepitaxially grown ZnO films on GaN substrates from 78 to 500 K (red circles), taken from Gaskins et al.<sup>[27]</sup> The measured values of  $h_K \approx 490 \text{ MW m}^{-2} \text{ K}^{-1}$  for ZnO/GaN is nearly a factor of 2 greater than the values predicted by both AGF and DMM at higher temperatures. The disagreement between theory and experiment points to the failure of the basic assumptions governing these theoretical frameworks. Specifically, since both AGF and DMM models are based on the harmonic approximation, the potential existence of anharmonic interactions of phonons and their contribution to enhancing  $h_K$  at this ZnO/GaN interface could be the cause for the discrepancies between the model and the data. Anharmonic channels with inelastic phonon transmission involving multiple phonon scattering events at the interface can open up additional channels for heat to traverse across the interface, thus, leading to an increase in the experimentally determined  $h_K$ .<sup>[32,34,49,53,55,72,73]</sup>

Since AGF at interfaces between two 3D solids has only been implemented in this harmonic limit, anharmonic AGF at realistic interfaces must be developed to study these inelastic phenomena properly. Additionally, the DMM and other phonon gas-based models cannot account for the atomistic nature of the

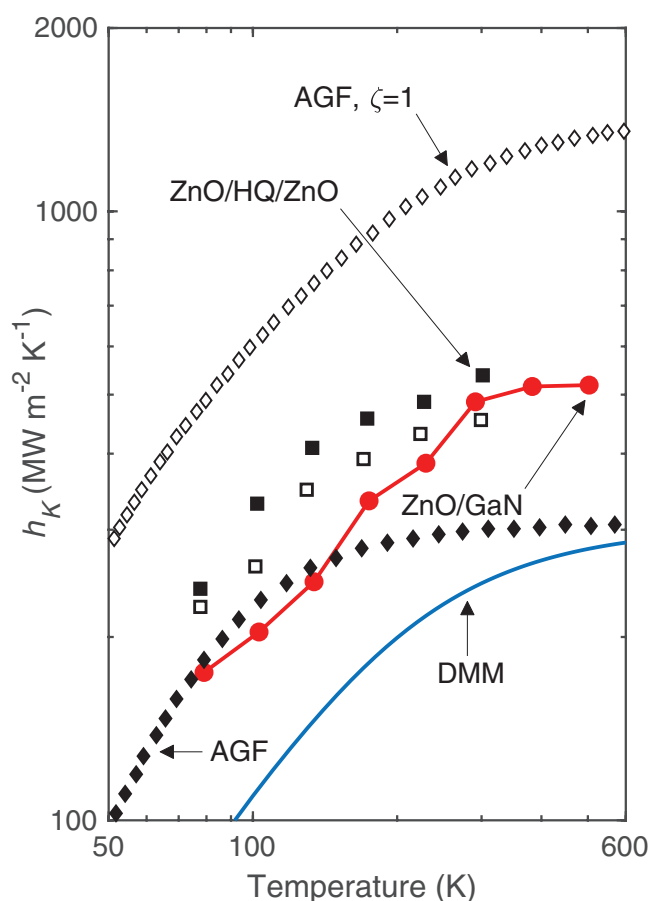


**Figure 4.** Measured thermal boundary conductance as a function of temperature for ZnO/GaN (solid circles) compared to data measured across ZnO/hydroquinone (HQ)/ZnO interfaces.<sup>[27,28]</sup> Predictions from the DMM and AGF for ZnO/GaN  $h_K$  (solid line and diamond symbols, respectively). The maximum  $h_K$  predicted across an ideal ZnO/ZnO interface from the AGF calculations (open diamond symbols) are also shown for comparison.<sup>[27]</sup> The agreement between the AGF and the ZnO/GaN data at low temperatures is because of the relatively higher contributions from long wavelength modes, which also explains the discrepancy with the DMM. At higher temperatures, the disagreement between data and the models that are rooted in the harmonic approximation suggests that inelastic channels of heat flow could be contributing to the  $h_K$  across ZnO/GaN interface at these temperatures.

solids adjacent to the interface. It has been shown that phonon interactions in this near interfacial region are critical for anharmonic mode conversions across interfaces to open up these additional inelastic scattering channels to thermal boundary conductance.<sup>[74]</sup> Thus, based on their underlying formalism, semiclassical phonon gas models cannot properly account for inelastic phonon processes on thermal boundary conductance.

It is interesting to note the convergence of the AGF-predicted thermal boundary conductances and those measured for the ZnO/GaN interface at low temperatures. Recall the work by Hua et al.'s<sup>[43]</sup> that experimentally demonstrated the increased interfacial heat flux from low frequency modes (Figure 3) as compared to that predicted by the DMM. At low temperatures, the phonon population will shift to lower frequencies as compared to elevated temperatures, and thus, the

thermal boundary conductance will be more so dominated by the lower frequency phonons. The AGF formalism accounts for the wave-like nature of phonon transport and can account for long wavelength phonons that efficiently transfer energy across interfaces more so than short wavelength phonons. This is in contrast to the DMM, which assumes all phonons scatter diffusively at interfaces, therefore under-predicting the contribution of long wavelength phonons to thermal boundary conductance. As such, the agreement of the experimental data with AGF and the disagreement with DMM at low temperatures is not surprising since long wavelength phonons dominate  $h_K$  at low temperatures.

The theoretical maximum thermal boundary conductance predicted under the AGF with the transmission coefficient equal to unity leads to a large contribution from higher frequency phonons that have a reduced transmission coefficient otherwise. The large over-prediction of the theoretical maximum compared to the data for ZnO/GaN in Figure 4 leads to the conclusion that long wavelength phonons have high efficacies of energy transfer across the interface while higher frequency modes are not as effective in carrying heat across the ZnO/GaN interface.

That the data for ZnO/GaN interface agrees with previously derived  $h_K$  from measurements of ZnO/hydroquinone (HQ) superlattices,<sup>[28]</sup> where the conductance across a ZnO/HQ/ZnO interface is only limited by the phonon flux in the ZnO,  $h_{K,ZnO/GaN}$  may not necessarily be related to the transmission of modes restricted by the modes on the other side of the interface and most likely is dictated by the phonon modes in the ZnO only. Thus,  $h_K$  may not be as strongly dictated by mode matching in the GaN, which is a principle assumption of Landauer formalism-based models. It is important to note that these results may also be explained by the presence of anharmonic interactions at the interface as pointed out above; however, with the data presented in Figure 4, it is not possible to claim which of the two mechanisms, or a combination of both mechanisms that are responsible for the differences between experiment and computation. The ability to perform more detailed measurements of the spectral contribution of various modes to thermal boundary conductance will be an important development moving forward.

#### 4. Harmonic Lattice Dynamics, Green's Function Approach and First-Principles Method to Calculate Interface Transport

We now briefly present some of the recent computational tools used to study interfacial heat transfer from an atomistic perspective. In this regard, the harmonic lattice dynamics (LD) calculations are the first computational approaches that successfully incorporated atomistic details by considering the structures and interatomic potential of the two materials in contact.<sup>[75]</sup> Both harmonic lattice dynamics and wave packet simulations are reciprocal-space based methods that describe the dynamics of phonons in an entire Brillouin zone under the harmonic approximation.<sup>[75–78]</sup> These works are important since they paved the way for more complex MD simulations that have become more popular and sophisticated recently (and will be discussed in Section 5). Both the LD and wave packet

methods can provide frequency dependent phonon reflection and transmission coefficients giving insights into the mode conversion processes occurring at the interface. As these simulations are performed in the harmonic approximation, there exists a direct correlation between the transmission coefficient and the ratio of the vibrational DOS of the two crystals.<sup>[76]</sup>

For the wave packet simulations, a linear combination of normal modes with  $\tilde{k}$  centered around a Gaussian is implemented in MD simulations so that the wave packet is localized in real space. The wave packet is allowed to propagate in a certain direction perpendicular to the interface and upon reaching the interface, the wave packet is either transmitted to the other side or reflected into the material of origin. The amplitudes of the normal modes at different times are recorded from which the phonon transmissivity is obtained. Thus, the wave packet method involves the extraction of mode transmissivities from MD simulations, but one of the requirements is that all other modes have zero amplitude, which essentially corresponds to a  $T = 0$  K simulations.<sup>[79–81]</sup> As such, these simulations are unable to capture the physics involved with temperature dependent anharmonic effects and therefore these simulations essentially reproduce the results from harmonic LD calculations.<sup>[76]</sup>

The atomic Green's function approach to calculate  $h_K$  is based on a system of classical harmonic Newtonian equations with solutions that are in the form of plane waves.<sup>[82]</sup> From the calculated Green's function matrix, it becomes possible to calculate the mode-dependent interface transmission coefficients for various types of interfaces.<sup>[83–86]</sup> This approach was pioneered by Mingo and Yang, where they calculated the diffusive to ballistic crossover for Si nanowires with amorphous coatings.<sup>[87]</sup> Since then, a number of studies have investigated thermal boundary conductance across a wide array of material interfaces, including phonon transport for graphene with grain boundaries,<sup>[88,89]</sup> interfacial transport across the technologically relevant Si/Ge heterostructures,<sup>[90,91]</sup> and two dimensional crystals such as MoS<sub>2</sub>, graphene nanoribbons, and single layer phosphorene.<sup>[92–94]</sup> Although a useful tool to calculate the thermal transport properties of various types of material systems, the AGF method is usually carried out in the harmonic approximation similar to the lattice dynamics approach. As such, AGF is mainly suitable for low temperatures where inelastic processes have negligible contribution to thermal transport. A comprehensive review of the AGF technique used to study interfacial transport is provided by Sadasivam et al.<sup>[84]</sup>

First-principles calculations to describe thermal transport across interfaces have been a relatively new approach mainly because of the extensive computational costs required to perform these calculations.<sup>[95–97]</sup> However, this approach holds promise in accurately describing all the different energy carrier dynamics, namely, electron, phonon, and magnon (and the cross interactions between these different energy carriers) across interfaces. So far, only a handful of studies (including a recent study conducted by the authors of this review) have utilized this approach to study interfacial transport.<sup>[96]</sup> Sadasivam et al.<sup>[95]</sup> used first-principles calculations to calculate the Eliashberg function describing the electron–phonon interactions for a TiSi<sub>2</sub>/Si supercell from which they estimated an effective electron–phonon conductance across the TiSi<sub>2</sub>/Si interface. They compared their results with the phonon-dominated



conductance predicted using the DMM and the theoretical maximum conductance (as discussed in more detail in Section 10). Although this work did not calculate all the energy conversion and scattering mechanisms across the interface with parameter-free first-principles calculations only, the first-principles approach has no limitations and in theory holds the promise to fully describe any energy exchange processes occurring at the interface. Recently, first-principles has also been used to calculate interfacial force constants between materials so as to accurately describe the vibrations at the interface, which are then used as input parameters for harmonic AGF calculations.<sup>[27,98]</sup> Doing so prevents errors that are inevitable in calculations that use simple averages of interfacial force constants to determine  $h_K$ .<sup>[99]</sup>

Even though all of the above mentioned approaches account for the atomistic nature of the interface, so far these techniques are only carried out in the harmonic approximation. Although these approaches have been shown to successfully describe the phonon modes that arise near an interface, accurately predicting the transport properties requires the inclusion of inelastic and anharmonic processes occurring at and near the interface. Therefore, more robust formalisms that are not reliant on the harmonic approximation are needed to fully capture the dynamics of these physical processes. An avenue for predicting interfacial transport that takes into account the anharmonic nature of the scattering processes without any limitations on the inelastic pathways for energy transport is MD simulations, which will be described in the following section.

## 5. Advances in Molecular Dynamics Simulations to Study Thermal Boundary Conductance

Unlike the semiclassical and atomistic lattice-dynamics based methods (including the AGF) used to study interfacial energy transport, the formalism of MD simulations does not require a priori understanding of heat transport. Furthermore, MD simulations have anharmonicity inherently built in based on the assumed potential and therefore includes inelastic effects due to multiple phonon interactions, rendering it a useful tool to study thermal boundary conductance across various types of material systems. However, classical MD does have the limitation of not being able to capture the quantum statistics since all the vibrational modes in a solid are excited.<sup>[100]</sup> Therefore, MD is mostly suited to study vibrational transport in a regime where the majority of the phonon modes participating in energy transport are thermally excited. Another major issue with MD simulations is the limitation on the size of the computational domain and the finite time scales for simulations. Moreover, since electron dynamics cannot be directly incorporated in MD, electrical conductors and electron–phonon coupling effects in solids cannot be investigated with a pure MD approach.

For systems in which the above mentioned limitations do not apply or have negligible influence on the physical mechanisms, MD simulations present a robust way to study interfacial transport with very large computational domains of atoms. In this regard, interfacial thermal transport has been mainly studied via either the equilibrium MD simulations with the

Green–Kubo approach<sup>[101,102]</sup> or the nonequilibrium MD simulations based on the “direct” method of applying heat baths on a computational domain and determining the temperature drop at the interface.<sup>[103,104]</sup> A comprehensive review of the two methods is provided by Schelling et al.<sup>[105]</sup> Variations and modifications of these two methods have resulted in computational tools that are able to calculate the modal or the spectral decomposition of heat current across interfaces.<sup>[73,106–112]</sup> Some of the most notable results and advances in our knowledge of interfacial transport through these methods will be discussed below, as this analysis approach represents a relatively new technique to advance our understanding of phonon thermal transport across interfaces.

In MD simulations, silicon and germanium have become prototypical systems for studying interfacial heat transfer, largely due to the availability of reliable interatomic potentials that can correctly replicate their vibrational as well as structural physics.<sup>[113–117]</sup> MD simulations naturally include all microscopic details at the interface including anharmonicity, which is not included in the formulations based on the harmonic approximations described in the previous section. As pertaining to the interfacial physics, Murakami et al.<sup>[60]</sup> have demonstrated the existence of interfacial modes in the local DOS for Si/Ge systems that are otherwise absent in the bulk DOS for each of the corresponding material; calculations based on the generic DMM and AGF methods cannot account for these types of interfacial modes that occur due to the anharmonicity in the system.

The interfacial modes in a Si/Ge system are shown in Figure 5a (adapted from Murakami et al.<sup>[60]</sup>), where the DOS for the first, second, and third atomic layers in either side of the interface are shown. It is interesting to note that modes that are above the cutoff frequency for Ge appear on the first atomic layer adjacent to the interface in Ge. Similarly, modes at the 12 to 13 THz also appear on the interfacial layer on the Si side that are not present on the DOS for bulk Si. The existence of interfacial modes for Si/Ge and their visualization with eigenvectors and their localization at the interface between Si and Ge are clearly depicted in Figure 5b,c for modes at 12.01 THz (figure taken from Gordiz and Henry<sup>[58]</sup>). The frequency of these interfacial modes are above the maximum frequency of the softer solid (Ge), which means any contributions to heat transfer across the interface by these modes is a result of the system’s anharmonicity. Before we discuss how these modes contribute to interfacial heat transfer, we will briefly review the spectral and modal decomposition methods applied for such calculations.

Tremendous progress has been achieved in terms of deconvolving the spectral- and/or mode- level contributions to interfacial thermal conductance between two solids in MD simulations. Most notably, the works from Chalopin and Volz<sup>[106,118]</sup> laid the foundation for more recent works by analyzing the energy transmission function from equilibrium fluctuations and calculating contributions of resonant interfacial modes to the thermal conductance. In general, for the mode-level detail of interfacial heat transfer, the heat flux  $Q$  between an atom  $i$  and  $j$  in materials  $A$  and  $B$ , respectively, is proportional to the correlation between the interatomic force ( $\vec{F}$ ) between the atoms and the velocities ( $\vec{v}$ )<sup>[119–122]</sup>



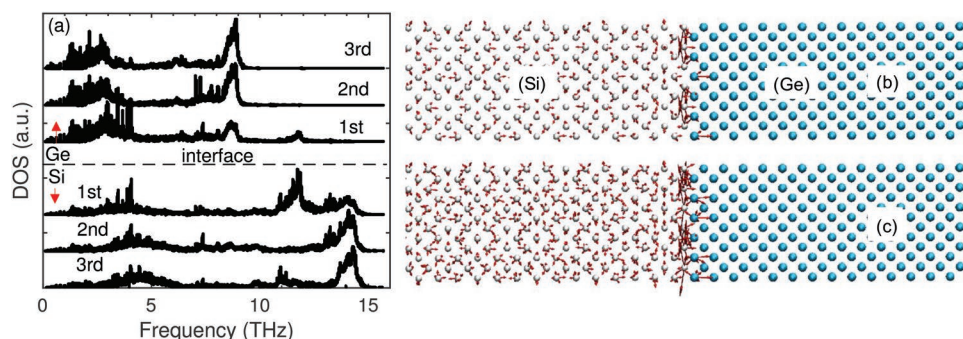


**Figure 5.** a) Local phonon density of states of the first, second and third atomic monolayers from a Si/Ge interface on either side. Evidence of interfacial vibrations in Si and Ge are observed near the interface that are not present in the bulk density of states. Eigenvectors for interfacial modes at b) 12.01 THz and c) 12.01 THz. Reproduced with permission.<sup>[58]</sup> Copyright 2016, AIP Publishing.

$$Q_{A \rightarrow B} = -\frac{1}{2} \sum_i \sum_j \tilde{F}_{ij} \cdot (\tilde{v}_i + \tilde{v}_j) \quad (5)$$

This equation only holds for pairwise interactions and a more general expression to include three and many-body interactions is given as<sup>[58,106,111]</sup>

$$Q_{A \rightarrow B} = -\sum_i \sum_j \left[ \frac{\tilde{p}_i}{m_i} \frac{-\partial H_j}{\partial \tilde{r}_i} + \frac{\tilde{p}_j}{m_j} \frac{-\partial H_i}{\partial \tilde{r}_j} \right] \quad (6)$$

where  $\tilde{p}_i$  is the momentum,  $m$  is the mass,  $\tilde{r}$  is the position, and  $H$  is the Hamiltonian. Using the above equations, studies have demonstrated the effectiveness of inelastic channels of heat transport across interfaces of Si/Ge,<sup>[58,60,106,111,123]</sup> InGaAs/InGaP,<sup>[124]</sup> and Lennard–Jones based systems,<sup>[57,61,73,107,110,123]</sup> which are not discernible via approaches based on the harmonic approximations. By considering full third-order force constants, Zhou et al.<sup>[123]</sup> have directly revealed the importance of three phonon scattering processes at interfaces for bulk Ar, Ar/heavy Ar, and Si/Ge systems.

These studies have emphasized that the description of heat transfer across interfaces cannot be accurately depicted by only considering just the bulk phonon properties of the constituent materials comprising the interface, and thus the concept of a phonon transmission across an interface between two materials breaks down. Therefore, it becomes imperative to consider the localized and nondispersive interfacial modes to accurately describe  $h_K$ . This is clearly shown in **Figure 6** (adapted from Gordiz et al.'s<sup>[58]</sup> work), where the spectral contributions with and without considering interfacial modes to  $h_K$  across Si/Ge are plotted. When considering the interfacial modes in their calculations, they show a sharp increase in the interfacial conductance for modes in the 12 to 13 THz range that contribute almost  $\approx 15\%$  to the total  $h_K$  even though they comprise  $<3\%$  of the total available modes in the whole system. Moreover, Gordiz and Henry postulate that these interfacial modes in the narrow 12 to 13 THz range can substantially facilitate heat transfer across the interface among other phonon modes since the conductance decreases when these interfacial modes are excluded from their calculations as shown in **Figure 6**.

Similarly, Feng et al.<sup>[111]</sup> used a modal decomposition technique to show that inelastic channels contribute  $\approx 45\%$  to  $h_K$  by

including the bulk regions along with the interfacial region in their calculations. Their results are shown in **Figure 7** where they calculate the spectral contributions both on the Ge and Si sides. They show that the spectral heat fluxes on the Si and Ge sides overlap with each other in the range of 0 to 5 THz, which indicates that elastic scattering dominates in this frequency range. They compare their results to AMM calculations (as shown in **Figure 7** with dashed line), which cannot replicate their results of the simulations at any frequency range even though the interface they consider is planar and clean. This suggests that the crude assumptions involved with the AMM cannot be applied to these interfaces even though the total  $h_K$  predicted by the AMM agrees well with the value predicted via NEMD simulation. Further, this shows the power of spectral

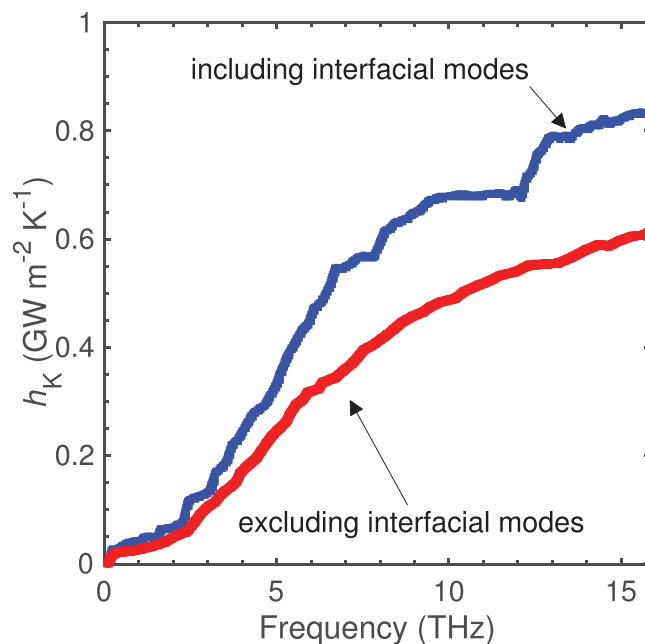


**Figure 6.** Spectral thermal boundary conductance accumulation for a Si/Ge interface with and without considering the interfacial modes as calculated by Gordiz and Henry.<sup>[58]</sup> The overall conductance is substantially under-predicted if the interfacial modes are excluded from the calculations. These simulations were conducted assuming a Tersoff potential to describe the silicon and germanium.<sup>[113,114]</sup>

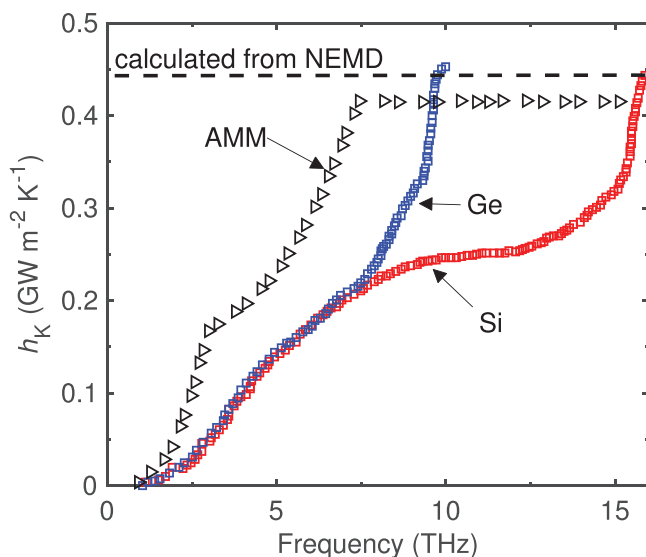


**Figure 7.** Spectral contributions to thermal boundary conductance as calculated by Feng et al.<sup>[111]</sup> for Si/Ge where the conductances are decomposed eight unit cells away from the interface at both sides so that the bulk modes and eigenvectors are also considered for the modal and spectral decomposition. These simulations were conducted assuming a tersoff potential to describe the silicon and germanium.<sup>[113,114]</sup>

decomposition to study the energy transport pathways across interfacial regions at heteromaterial junctions, as it gives insight into specific mode conversions that can occur from the abrupt changes in atomistic masses and forces near an interface. While previous theoretical<sup>[49]</sup> and MD-based<sup>[74]</sup> works have predicted similar near-interfacial processes could be driving inelastic transport in thermal boundary conductance, the use of modal decomposition to study this process provides a deeper level of insight.

To further exemplify the importance of inelastic pathways affecting interfacial heat transport, we show calculations by Giri et al.<sup>[110]</sup> of normalized spectral heat current accumulation from Lennard–Jones based Solid A ( $m = m_{Ar}$ ) to Solid B ( $m = 4m_{Ar}$ ) as depicted by the schematic in the top panel of **Figure 8a**. Calculations for a range of cross-species interaction strengths ( $\epsilon_{A-B}$  in the range  $\epsilon_{Ar}$  to  $\epsilon_{A-B}/4$  as shown in **Figure 8a**) conducted at 30 K are plotted for comparison. **Figure 8a** also shows the predictions for the case with  $\epsilon_{A-B} = \epsilon_{Ar}$  which is the relatively strongly bonded interface, conducted at 1 K temperature to effectively reduce inelastic effects. The heat flux accumulation from Solid A to Solid B has negligible contributions from frequencies greater than the cutoff frequency of Solid B, even though the cutoff frequency of Solid A is twice that of Solid B. In contrast, frequencies greater than the cutoff frequency of Solid B contribute to more than 50% of the total heat flux from Solid A to Solid B for the strongly bonded interface at the higher temperature. This can be understood by considering anharmonic channels and inelastic phonon scattering processes that significantly affect interfacial heat flow at higher temperatures; where harmonic interactions limit the accumulation to reach 100% by the maximum frequency in Solid B, anharmonic interactions open up channels for heat conduction, thereby allowing modes with different frequencies to

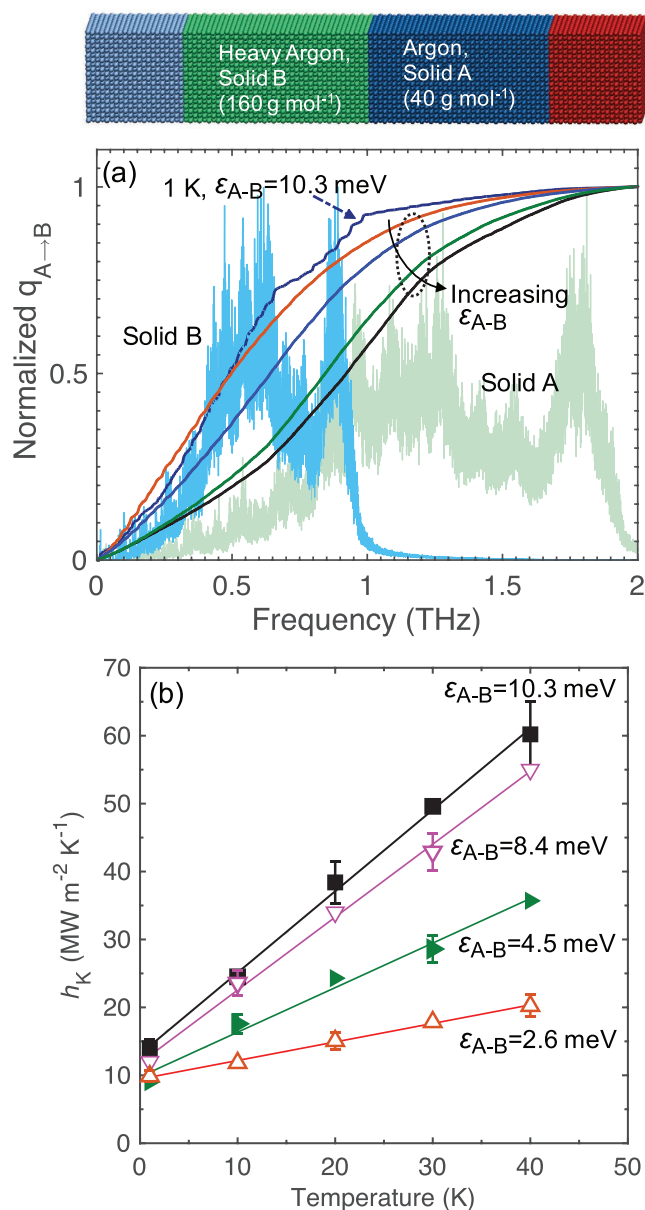


**Figure 8.** a) Top panel: Schematic of the computational domain for Ar/heavy-Ar system. Bottom panel: Normalized thermal boundary accumulation at 30 K for a Ar/heavy-Ar system with varying interfacial bond strength  $\epsilon_{A-B}$ . Also included is the accumulation calculated at 1 K, which represents the harmonic limit for the computational domain with  $\epsilon_{A-B} = 10.3$  meV. The density of states of the bulk solids are shown in the background to emphasize the relative cutoff frequencies in the solids. b) Temperature dependent thermal boundary conductance predicted via nonequilibrium molecular dynamics simulations for a range of cross-species interactions  $\epsilon_{A-B}$ .

interact.<sup>[26,34,49,51,53,55,73,107,125]</sup> Although anharmonicity decreases thermal conductivity of homogeneous crystals due to multiple phonon scattering processes that add resistance, heat conduction across interfaces is aided by anharmonicity as is suggested in **Figure 8a** by the increase in the spectrum of frequencies in Solid A that can carry heat across the interface at higher temperatures.<sup>[110]</sup>

It is also interesting to note that in comparison to the strongly bonded case with  $\varepsilon_{A-B} = \varepsilon_{Ap}$  the weaker strength of cross-species interactions leads to a shift from mid-frequency phonons dominating heat flow to lower frequencies contributing the most to the heat flux from Solid A to Solid B. This is shown by the gradual shift to lower frequencies with decreasing interaction strengths across the interface in Figure 8a. Furthermore, inelastic channels are inhibited for the interface with the weakest cross-species interaction as evidenced from the negligible contribution to the total heat flux from phonon frequencies higher than the cutoff frequency of Solid B. This is further quantified by the temperature dependencies of  $h_K$  predicted via NEMD simulations across the Solid A/Solid B interface for the various  $\varepsilon_{A-B}$  as shown in Figure 8b. As the strength of interaction across the interface is reduced, the increase in  $h_K$  with temperature gradually becomes less pronounced. At low temperatures,  $h_K$  values converge for all the interaction strengths suggesting that anharmonic phonon scattering processes that increase  $h_K$  with temperature for the strongly bonded case are inhibited for the weakly bonded case and this inhibition is less pronounced at lower temperatures where inelastic interactions are limited, in line with the spectrally decomposed heat flux shown in Figure 8a and consistent with another previous work on these types of Lennard–Jones solids.<sup>[126]</sup>

## 6. Thermal Conductance of Interfaces with Amorphous Materials

In practical applications that utilize sputtering or evaporation techniques resulting in non epitaxial film deposition, disorder and film oxidation at interfacial layers between two solids (e.g., metal-oxide-semiconductor structures containing silicon include a nonstoichiometric oxide layer present at the Si/SiO<sub>2</sub> interface)<sup>[128]</sup> can introduce additional resistance to thermal transport. This disruption of crystallinity in thin films can influence the material's vibrational characteristics, which in turn influences the thermal boundary conductance across thin films. Unlike in crystalline solids, vibrations in amorphous and disordered materials are classified as propagons (that are delocalized, propagating modes), diffusons (that are nonpropagating, delocalized modes), and locons (that are localized and nonpropagating modes).<sup>[129]</sup> Note, while locons do not contribute to the thermal conductivity, diffusons mediate heat through harmonic coupling of vibrations in a highly disordered solid.<sup>[130,131]</sup>

Interfacial conductance across highly disordered interfaces has not received as much attention mainly due to limited experimental capabilities and theoretical models to analyze the heat transport mechanisms. In comparison, interfacial transport across crystalline interfaces have been extensively studied with well-established models and robust experimental techniques, which have led to significant physical insights as discussed above.<sup>[2,39]</sup> Quantifying  $h_K$  across amorphous interfaces in comparison to their crystalline counterparts is difficult due to the low thermal conductivity of the amorphous layers, which results in a negligible temperature drop across the interface that becomes hard to determine with low uncertainties both experimentally and computationally.<sup>[127,132]</sup>

Giri et al.<sup>[127]</sup> have sought to overcome the challenges associated with accurately determining the negligible temperature drop across interfaces formed between amorphous layers by computationally investigating Stillinger–Weber based amorphous Si/Ge superlattices via MD simulations; an example of their superlattice structure is shown in Figure 9a. With a large number of interfaces posing resistance to heat flow in series, they are able to accurately predict the conductance across a single interface using a thermal circuit model. Their results show that the conductance can be as high as  $\approx 2 \text{ GW m}^{-2} \text{ K}^{-1}$  across amorphous interfaces. Similar high conductances across amorphous interfaces have also been predicted by Gordiz et al.<sup>[133]</sup> via MD simulations. For crystalline interfaces, MD results show that  $h_K$  can be lower than up to a factor of 5 compared to the conductance across their amorphous counterparts.<sup>[104,127,133]</sup> This difference in conductances is despite the fact that the vibrational mismatch between the amorphous and crystalline phases of Si and Ge are very similar as shown in the DOS plotted for the different phases of Si and Ge in Figure 9b. Although the vibrational bandwidths are similar regardless of their phases, the dominant vibrations that carry heat in the crystalline and amorphous phases are very different. For the case of the amorphous superlattices, the dominant heat carrying vibrations in the Si and Ge layers are nonpropagating modes (diffusons), whereas, spatially extended modes predominantly contribute to thermal transport in the crystalline counterparts.

In the experimental side, techniques such as TDTR and FDTR that have been used to study crystalline interfaces do not provide sufficient sensitivity to accurately quantify  $h_K$  across amorphous interfaces as mentioned in the above paragraph. Using a different thermometry technique that utilizes the temperature of magnetic thin films, Kimling et al.<sup>[17]</sup> determine a high value of  $>0.6 \text{ GW m}^{-2} \text{ K}^{-1}$  for an amorphous SiO<sub>2</sub>/crystalline Si interface. Similarly, motivated by their computational findings as described in the above paragraph, Giri et al.<sup>[35]</sup> also demonstrate an ultrahigh conductance across amorphous/amorphous interfaces experimentally by utilizing amorphous multilayer structures. Similar to their procedure in their MD study,<sup>[127]</sup> they measured the thermal conductivity as a function of interface density (or period length) by TDTR and used a resistor model to determine the conductance across an individual interface as shown in Figure 9c,d. Their SLs are composed of hydrogenated amorphous silicon carbide (a-SiC:H) and hydrogenated silicon oxycarbide (a-SiOC:H) that are investigated due to their unique characteristics that are of technological and scientific importance, especially as low-k dielectric materials.<sup>[134,135]</sup> Ultrahigh conductance is demonstrated at amorphous SiOC:H/SiC:H interfaces, approaching  $1 \text{ GW m}^{-2} \text{ K}^{-1}$  and are further increased through the introduction of nitrogen defects that add interfacial modes, which lead to higher interfacial conductances across these disordered interfaces. To support the hypothesis that interfacial modes exist due to the nitrogen defect atoms at the interfacial regions between the layers, Giri et al. also conducted supercell lattice dynamics calculations of DOS as shown in Figure 9e. Their results show that the introduction of defect atoms leads to a pronounced increase in the DOS of interfacial modes. This is further supported experimentally with subtracted FTIR spectra for samples with and without nitrogen defect atoms

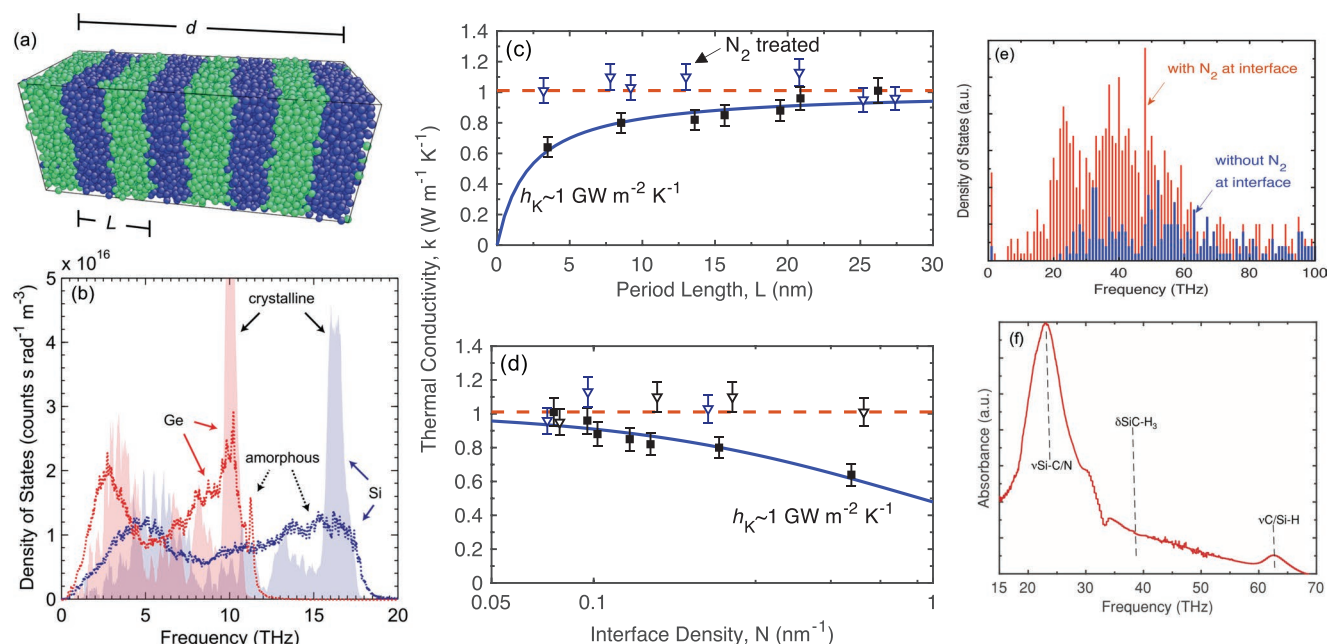


**Figure 9.** a) Schematic of a computational domain for a Stillinger–Weber based amorphous superlattice where blue and green atoms represents Si and Ge, respectively. Reproduced with permission.<sup>[127]</sup> Copyright 2015, AIP Publishing. b) Vibrational density of states for different phases of Si and Ge taken from Giri et al.<sup>[127]</sup> Thermal conductivities of amorphous SiOC:H/SiC:H superlattices as a function of c) period length and d) interface density as adapted from Giri et al.<sup>[35]</sup> The solid circles represent superlattices without the nitrogen defect atoms at the interfacial regions and the hollow triangles represent superlattices with nitrogen defect atoms at the interfacial regions. The nitrogen defect atoms are shown to increase the thermal conductivities of superlattices with smaller period thicknesses suggesting that the interfacial resistances are negligible for these superlattices. e) Lattice dynamics calculations of density of states for interfacial modes as defined by Gordiz and Henry<sup>[57]</sup> for an amorphous SiOC:H/SiC:H superlattice. The presence of nitrogen atoms in the interfacial region leads to the formation of localized modes near the interface. f) Subtracted FTIR spectra for SiC:H/SiOC:H multilayers with nitrogen defect atoms at the interface with respect to another sample without the nitrogen defect atoms. FTIR shows similar enhancement of vibrational modes at the 15 to 50 THz range as determined from the lattice dynamics calculations.

showing similar increase in vibrations at these frequencies with nitrogen defect atoms at the interface (see Figure 9e).

The existence of interfacial modes has also been experimentally observed via high-energy resolution monochromated electron energy loss spectroscopy systems for interfaces between crystalline Si and amorphous  $\text{SiO}_2$ .<sup>[59]</sup> Their results show that localized modes at  $\approx 33.3$  THz that corresponds to Si–O bond stretching exists in the Si side a few nanometers away from the interface even though these modes are nonexistent in the bulk Si. These results agree very well with MD calculations from Gordiz et al.<sup>[136]</sup> for the interface formed between crystalline Si and amorphous  $\text{SiO}_2$ . Gordiz et al.<sup>[136]</sup> also show that even though these modes comprise less than 5% of the total modes in the system, they can contribute to more than 15% of the total interfacial conductance. All of these works point to the fact that localized modes at the interface can significantly alter the interfacial conductance and should not be ignored while considering thermal transport in systems with broken symmetries introduced via interfaces.

## 7. Effect of Nanostructuring and Surface Functionalization

We now turn our attention to the extrinsic factors that control  $h_K$  across various types of interfaces. Kapitza conductance is extremely dependent on the structural details of the interface

at the nanoscale since the characteristic dimensions are comparable to or less than the vibrational mean-free paths. Nanostructuring at the interface has been efficiently used to tune the energy transport pathways across interfacial regions either by introducing roughness,<sup>[78,90,137,138]</sup> nonplanar features,<sup>[139–141]</sup> interface mixing,<sup>[137,142]</sup> or by functionalizing the interface to alter the stiffness of the bonds.<sup>[143–151]</sup>

Experimental works have demonstrated that nonplanar features of nanofabricated fin-like projections with characteristic length scales of  $\approx 100$  nm can substantially increase the interfacial heat flow through an increase in the overall contact area.<sup>[139,140]</sup> Similarly, MD studies have also shown that these types of features (even down to sub-nanometer length scales) can be used to achieve an increase in  $h_K$ .<sup>[78,141,152]</sup> This idea of nanopillars that increase the area for heat flow is analogous to the implementation of macroscale fin arrays used to increase the contact area of solids with the fluid environment.

One has to be careful while implementing such nanostructure engineering approaches at the interface to increase  $h_K$  since Hopkins et al.<sup>[67]</sup> have shown that  $\text{Ge}_x\text{Si}_{1-x}$  quantum dots grown on Si substrate can in fact lower  $h_K$  measured across Al/Si interfaces. This is in contrast to the effect of nanopillars at interfaces between Al/Si as experimentally shown by Lee et al.<sup>[140]</sup> where nanopillar spacings in the range of  $\approx 15$ –150 nm at Al/Si interfaces can drastically increase  $h_K$ . It is possible that the  $\text{Ge}_x\text{Si}_{1-x}$  alloy can lead to larger resistances due to its intrinsically lower thermal conductivity or that at some critical length scale or



root-mean-square roughness, surface features can transition from decreasing to increasing  $h_K$ . Additionally, other factors such as the alteration of the interfacial chemistry and bonding could also play a role.

Another approach to enhance  $h_K$  across interfaces is by altering the vibrational density of states at the interfacial region through engineering mass graded boundaries via intermixing of the species or by insertion of an interfacial film that bridges the vibrational properties of the two solids in contact.<sup>[65,90,103,137,153–155]</sup> In comparison to a sharp and abrupt interface, the compositionally disordered (and mass graded) interfaces can demonstrate enhanced  $h_K$  through vibrational impedance matching between the two solids along with opening new channels of heat transport via anharmonic interactions. For example, Hahn et al.<sup>[156]</sup> have shown that an alloy of  $\text{Si}_x\text{Ge}_{1-x}$  at the Si/Ge interface with a finite thickness of  $\approx 0.5$  nm can increase  $h_K$  by  $\approx 24\%$ . They attribute this enhancement to reduced lattice and mass mismatch between the pure Si and Ge solids, which results in a better vibrational impedance matching. However, a further increase in the thickness of the interfacial  $\text{Si}_x\text{Ge}_{1-x}$  alloy region resulted in lower  $h_K$  due to the dominant effect of alloy scattering intrinsic to the finite thickness interfacial region over the enhancement due to the reduction in the lattice and mass mismatch. Moreover, the functional form of the concentration profile of the intermixing region at the interface has also been shown to alter interfacial conductance.<sup>[137,154]</sup>

Although the majority of the work that have considered mass grading and compositional disorder at the interface have been computational, a few experimental works have also studied the effect of disorder on  $h_K$ . Hopkins et al.<sup>[65]</sup> studied Cr/Si interface for a variety of interfacial conditions and showed that  $h_K$  is influenced by the thickness of the mixing region and the rate of compositional change in the mixing region. Likewise, Gorham et al.<sup>[142]</sup> showed that ion irradiation of a native oxide interface can lead to an increase in  $h_K$  across Al/native oxide/Si interface. They show that under certain ion irradiation conditions the acoustic impedance mismatch between the Al and the native oxide is lower thus increasing the measured  $h_K$ . The atomic vibrational mechanisms that lead to this increase in  $h_K$  is currently unknown but provides a landscape for future studies. Another more recent study by Giri et al.<sup>[35]</sup> demonstrated that small mass defect atoms near the interface can lead to an increase in  $h_K$  through the increase in the density of states of interfacial modes that facilitates heat transfer across interfaces. Although these experimental results show that disorder and defects can be used to manipulate  $h_K$ , a direct comparison between computational works and experimental works can lead to significant new insights into the atomistic nature of interfacial heat transfer. Therefore, more material systems must be studied that can be judiciously fabricated to have a direct comparison with interfaces studied in computational works.

Surface treatment and functionalization at the interface has been another popular avenue to efficiently tune  $h_K$ . Losego et al.<sup>[150]</sup> experimentally demonstrated that by gradually changing interfacial interactions from weak van der Waals interactions to covalent bonding via self-assembled monolayers (SAMs) between Au and quartz,  $h_K$  can be increased by as much as  $\approx 80\%$ . Similar studies have been performed for

interfaces between metal/graphene/ $\text{SiO}_2$  where plasma functionalization is used to chemically modify graphene, which can result in a strongly bonded interface between the metal and graphene.<sup>[157–159]</sup> Typically, when changes in the surface chemistry such as with  $\text{O}_2$  or  $\text{N}_2$  functionalization that favors an increase in adhesion between the graphene and the metal,  $h_K$  can be notably improved.<sup>[157,160]</sup> For Au/Ti/Gr/ $\text{SiO}_2$  without any surface functionalization, an intrinsic  $h_K \approx 33 \text{ MW m}^{-2} \text{ K}^{-1}$  has been measured that is four times smaller than that of the Au/Ti/ $\text{SiO}_2$  interface.<sup>[161]</sup> Recent studies have also shown that  $h_K$  measured across Au/Ti/Gr/ $\text{SiO}_2$  and Au/Ti/ $\text{O}_x$ /substrate interfaces are not only impacted by the weak interfacial bonding, but are also significantly impacted by the oxide compositions at the Ti contacts that are highly dependent on the Ti deposition rate and base pressure.<sup>[162,163]</sup>

## 8. Thermal Boundary Conductance across Interfaces Composed of 2D Materials

The low conductances across graphene interfaces are typical of interfaces composed of 2D/3D interfaces mainly due to the weak interaction of the 2D layer with the substrate. Experimental methods such as Raman spectroscopy,<sup>[164–166]</sup> pump-probe thermoreflectance,<sup>[158,160,161]</sup>  $3\omega$  technique,<sup>[167,168]</sup> and more recently developed electrical thermometries<sup>[169,170]</sup> have been utilized to experimentally study thermal conductance across interfaces comprised of 2D materials. Most of these studies have focused on understanding heat transfer across graphene on a substrate, with reported  $h_K$  in the range of  $\approx 20$ – $35 \text{ MW m}^{-2} \text{ K}^{-1}$  for graphene on  $\text{SiO}_2$ , Si and AlN substrates.<sup>[158,161,169,171,172]</sup> However, it should be noted that the interfacial chemistry between the graphene and the substrate can significantly influence the heat transfer across these interfaces as mentioned in the preceding Section.<sup>[157,158,160]</sup> Furthermore, Freedy et al.<sup>[162]</sup> have shown that the  $h_K$  across Ti/Gr/ $\text{SiO}_2$  contacts that are mostly studied in literature, largely depends on the oxide composition at the contact. By varying the base pressure and the deposition rate of the encapsulating Ti layers, they show that the oxide composition in the Ti layer can be systematically changed. Their results suggest that a faster deposition rate leads to minimal oxide composition at the contacts thus significantly increasing the measured  $h_K$  as summarized in Figure 10a.

Similar to the reported values of  $h_K$  for interfaces with graphene, Yasaei et al.<sup>[169]</sup> measured the conductance across  $\text{MoS}_2$  on  $\text{SiO}_2$ /Si at room temperature via electrical thermometry technique and found  $h_K$  in the range of  $\approx 20.3$  to  $33.5 \text{ MW m}^{-2} \text{ K}^{-1}$  across the dimensionally mismatched interfaces. Similarly, Yalon et al.<sup>[164]</sup> reported a lower value of  $\approx 15 \text{ MW m}^{-2} \text{ K}^{-1}$  for  $\text{MoS}_2$  with AlN and  $\text{SiO}_2$  at room temperature, using Raman thermometry with laser-induced heating. A comparatively higher conductance of  $62.5 \text{ MW m}^{-2} \text{ K}^{-1}$  has been reported for metal-coated single-layer boron nitride on  $\text{SiO}_2$  substrate via a  $3\omega$  technique.<sup>[168]</sup> It was also shown that increasing the number of boron nitride layers (to a total thickness of 12.8 nm) led to a reduction of as much as  $\approx 50\%$  in the measured  $h_K$ .<sup>[168]</sup> Tungsten diselenide on  $\text{SiO}_2$  substrate showed similar thickness dependent behavior as reported by Behranginia et al.<sup>[165]</sup> via an electronic-heating Raman-probe platform. However, the

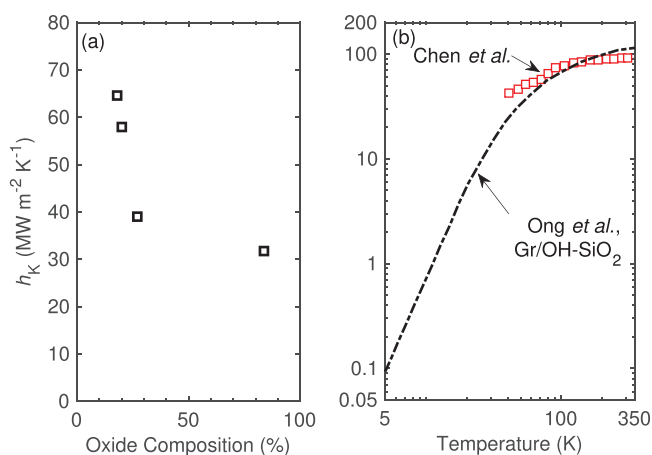


**Figure 10.** a) Experimentally measured thermal boundary conductance as a function of oxide composition at the interface. The thermal boundary conductance decreases as the oxide composition increases. b) Thermal boundary conductance predicted by Ong et al.<sup>[173]</sup> model that accounts for a top SiO<sub>2</sub> encapsulating layer, which increases the predicted  $h_K$  through additional channels of heat transfer as compared to the conductance across a bare graphene/SiO<sub>2</sub> contact. The model matches very well with the experimental results from Chen et al.<sup>[167]</sup>

conductance was shown to peak for 3 to 4 layers of WSe<sub>2</sub> with a value of 32 MW m<sup>-2</sup> K<sup>-1</sup>.

Beyond the measurements on the conventional graphene on substrate, Yasaei et al.<sup>[170]</sup> have measured  $h_K$  across a Ti<sub>3</sub>C<sub>2</sub>/SiO<sub>2</sub> interface, with an aluminum oxide encapsulating layer that can efficiently increase the rate of repopulation of the flexural modes in the 2D (Ti<sub>3</sub>C<sub>2</sub>) layer by removing the internal resistance in the layer between the longitudinal and transverse phonons to the flexural mode. They argue that this coupling in the layer is the rate limiting mechanism for interfacial heat flow and increasing the coupling can lead to higher values of measured  $h_K$  across Ti<sub>3</sub>C<sub>2</sub>/SiO<sub>2</sub>. Without encapsulation, the heat transfer is mainly limited by the internal resistance in the Ti<sub>3</sub>C<sub>2</sub> layer due to slow repopulation of low-frequency ZA modes via phonon–phonon interactions.<sup>[169]</sup>

To understand the low conductances associated with interfaces comprised of 2D materials, there have been considerable advances both from atomistic simulations<sup>[109,174–176]</sup> as well as analytical and theoretical frameworks.<sup>[50,125,173,177–180]</sup> One of the main findings from the MD simulations is that the conductance across the dimensionally mismatched graphene and substrate can be ascribed to the coupling between flexural acoustic phonons of graphene and the longitudinal phonons in the substrate.<sup>[109]</sup> The simulations show that the most efficient thermal transport channel across graphene/substrate interfaces is the transmission of energy from the acoustic branches (especially the flexural modes) in graphene to the cross-plane longitudinal acoustic and optical modes in the substrate.<sup>[109]</sup>

Likewise, analytical formulations have also alluded to the importance of flexural modes in conducting heat across 2D/3D interfaces. Persson et al.<sup>[179,180]</sup> derived a theoretical model for heat transfer that takes into account the dimensionality mismatch between a 2D crystal and a 3D substrate. In reasonable agreement with experiments, their theory predicts

$h_K = 25 \text{ MW m}^{-2} \text{ K}^{-1}$  between weakly coupled graphene/SiO<sub>2</sub>. However, their model does not consider the full phonon dispersion of the 2D layer, and treats the 2D material as an elastic membrane with perfectly quadratic flexural vibrational modes. Ong et al.<sup>[173]</sup> further modified this model by adding a top encapsulating layer, which increased the predicted  $h_K$  through additional channels of heat transfer via coupling of the low frequency flexural mode of the 2D crystal with the Rayleigh phonon modes from the encapsulating layer. Their model predictions are shown in Figure 10b for a graphene layer encased between SiO<sub>2</sub>. They show that by accounting for the spring constant between graphene and SiO<sub>2</sub> taking into consideration the OH– termination at the SiO<sub>2</sub>, their model matches well with the experimental results from Chen et al.<sup>[167]</sup> The importance of flexural modes of graphene and single layer MoS<sub>2</sub> on SiO<sub>2</sub> substrate was further highlighted in the work by Correa et al.<sup>[178]</sup> where the authors defined a heat flux across the interface by incorporating a phonon–substrate interaction rate and first-principles calculated phonon dispersion relations as input parameters in the model for phonon transport across interfaces composed of a monolayer supported on crystalline as well as disordered bulk substrates. In this work, the modification in the phonon dispersion relation for the ZA acoustic modes due to interaction with the substrate, which lifts the long wavelength modes near the Brillouin zone center, is accounted for thus capturing the physics and importance of the flexural modes.<sup>[178]</sup> Furthermore, a thorough review and calculations of  $h_K$  across six common 2D materials and seven substrates has also been carried out by Foss et al.<sup>[177]</sup> Along with the significance of the flexural modes, this study has emphasized the role of the substrate properties such as mass density and sound speed to be important factors while considering the heat transfer across 2D/3D interfaces.

## 9. Effect of Pressure and Bonding on Thermal Boundary Conductance

Mechanical strain can be used to modify the optical, thermal and electrical properties of materials.<sup>[181–186]</sup> High pressures can be used to increase the strength of bonds and stiffen the interface, which offers a novel pathway to control interfacial chemistry and therefore interfacial heat transfer.<sup>[187]</sup> In general, the application of hydrostatic pressure causes the spring constant that holds the atoms in their equilibrium position to increase. The increase in the spring constant is reflected by the hardening of the phonon frequencies as shown in Figure 11a for the case of Al at three different pressures calculated via density functional perturbation theory as implemented in the Quantum Espresso package.<sup>[188]</sup> These calculations by Giri et al.<sup>[184]</sup> show that the maximum frequency monotonically increases with increasing hydrostatic pressure along with the decrease in the heights of the high-frequency peaks in the DOS. Furthermore, as shown in Figure 11b by the phonon dispersion relations of Al calculated along high symmetry directions, the group velocities of the different polarizations increase substantially with pressure. Through MD simulations, Giri et al.<sup>[61]</sup> have shown that an increase in the group velocities of modes near an interface can greatly increase  $h_K$ .

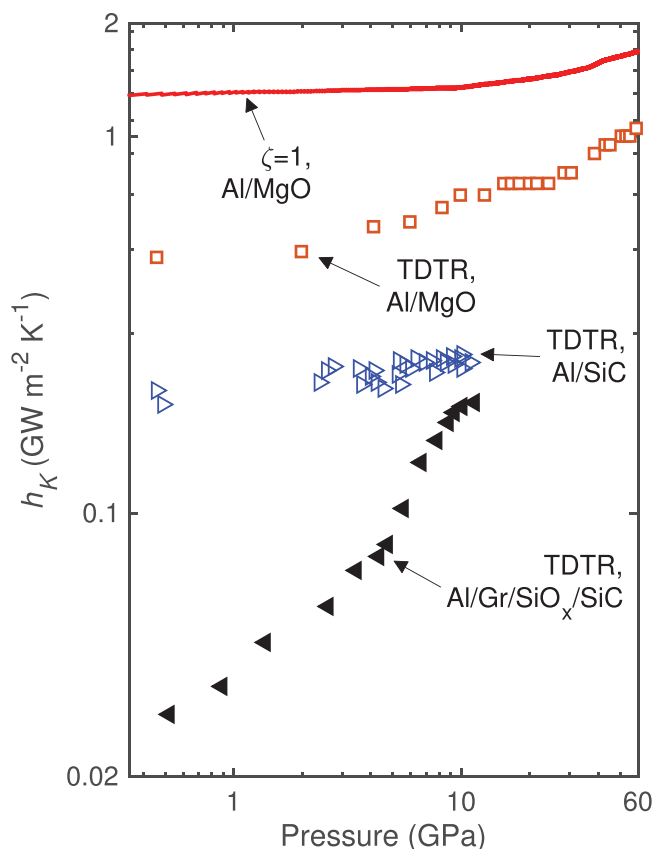


**Figure 11.** a) Bulk phonon density of states for Al at different hydrostatic pressures. b) Phonon dispersion of Al along high symmetry directions at ambient and 82 GPa pressures. c) Thermal boundary conductance versus pressure for Al/MgO,<sup>[25]</sup> Al/SiC, and Al/Gr/SiO<sub>x</sub>/SiC.<sup>[187]</sup>

The effect of high pressures on  $h_K$  has been studied via Anvil cell techniques.<sup>[19,25,187]</sup> Wilson et al.<sup>[25]</sup> have shown that  $h_K$  across Al/MgO interface increases monotonically from 0 to 60 GPa as shown in Figure 11c (red hollow squares). They show that even though the measured conductances are  $\approx 40\%$  lower than the maximum theoretical conductance calculated for Al,  $h_K$  increases at approximately the same rate as  $h_{K,\text{max}}$  for an ideal Al/Al interface. Similarly, with a SiC anvil cell, Hsieh et al.<sup>[187]</sup> have shown that the increase in  $h_K$  across a weakly bonded interface (as in the case of Al/graphene/SiO<sub>2</sub>/SiC) is more pronounced as compared to an interface that is strongly bonded (as in the case of Al film deposited on clean SiC) as shown in Figure 11c. They ascribe the linear increase of  $h_K$  to an increase in the average phonon transmission coefficient, which eventually approaches a large value when the majority of heat-carrying phonons are able to conduct heat across the interface; the saturation in the transmittance of phonons leads to the high values of  $h_K$  even at low pressures for the strongly bonded interface between Al deposited on clean SiC.

Hohensee et al.<sup>[19]</sup> studied  $h_K$  across various metal/diamond interfaces via diamond anvil cell and TDTR. They found that the conductance weakly depends on pressure and saturates at high enough pressures. They argue that anharmonic processes dictating the weak increase in conductance involves two phonons in diamond and one phonon in the metal, contrary to

two phonons in the metal decaying to one phonon in the diamond that would lead to a stronger pressure dependence. Such anharmonic scattering processes dictating  $h_K$  have also been proposed theoretically and observed via MD simulations.<sup>[55,73]</sup>

## 10. Effect of Electron Scattering on Thermal Boundary Conductance

In metals, the dominant energy carrier is the electronic subsystem that can be perturbed to highly nonequilibrium states following short-pulsed laser excitations. Theoretical and computational studies have employed the two-temperature model<sup>[189]</sup> that describes the temporal and spatial evolution of the electronic and lattice temperatures during ultrafast laser heating. The absorption of the laser pulse by the metal surface and the subsequent energy relaxation processes thereafter can be described by three characteristic time intervals: i) the thermalization of the free electron gas, ii) the coupling between electrons and the lattice; and iii) the energy transport driven by the gradient in the lattice temperature.<sup>[190]</sup> At an interface between two metals,  $h_K$  is dominated by electrons and therefore have ultrahigh conductances that are more than an order of magnitude larger than the values for phonon-dominated  $h_K$ . For example, Gundrum et al.<sup>[37]</sup> reported  $h_K \approx 3.7 \text{ GW m}^{-2} \text{K}^{-1}$  across Al/Cu interfaces at room temperature; their results are shown in Figure 12 for the 78 to 300 K temperature range (solid diamond

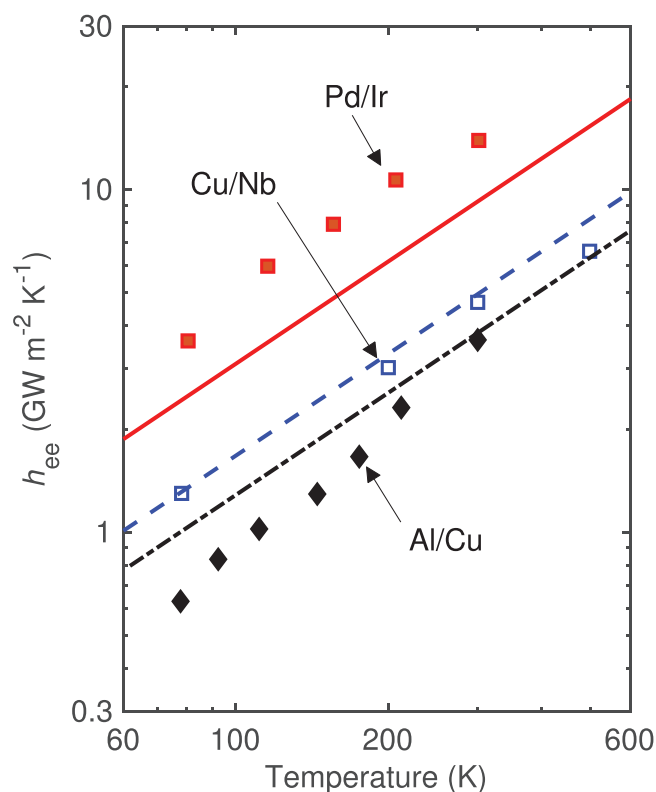


**Figure 12.** Temperature dependent thermal boundary conductances measured for Cu/Nb,<sup>[36]</sup> Pd/Ir,<sup>[38]</sup> and Al/Cu.<sup>[37]</sup> Similar trends are also shown from the respective calculations of electron-dominated conductances from the diffuse mismatch model.

symbols). Similarly, Wilson and Cahill measured the highest ever reported  $h_K$  for a solid/solid interface ( $\approx 12.1 \text{ GW m}^{-2} \text{ K}^{-1}$ ) for a Pd/Ir interface at room temperature (solid red squares). Cheaito et al.<sup>[36]</sup> also reported large conductances for Cu/Nb interfaces as shown in Figure 12 (hollow blue squares). While all of these studies report ultrahigh values of  $h_K$ , they also report a linear increase in  $h_K$  with temperature. They explain this linear trend through the DMM for electrons given as<sup>[36]</sup>

$$h_{ee,1 \rightarrow 2} = \frac{1}{4} \zeta_{1 \rightarrow 2} C_{e,1} v_{F,1} = \zeta_{1 \rightarrow 2} \frac{\partial q_1}{\partial T} \quad (7)$$

where  $C_{e,1}$  is the electronic heat capacity of the metal given as<sup>[191]</sup>  $C_{e,1} = (\pi^2/3) D(\epsilon_F) k_B^2 T$ , where  $k_B$  is Boltzmann's constant,  $q_1$  is the electronic flux on side 1, and  $\zeta_{1 \rightarrow 2}$  is given by<sup>[37]</sup>

$$\zeta_{1 \rightarrow 2} = \frac{D(\epsilon_{F,2}) v_{F,2}}{D(\epsilon_{F,2}) v_{F,2} + D(\epsilon_{F,1}) v_{F,1}} \quad (8)$$

where  $D(\epsilon_F)$  is the density of states at the Fermi level and  $v_F$  is the Fermi velocity. Figure 12 shows the calculations of the electronic DMM, which agrees qualitatively well with the experimental data and the temperature trends of the experimental data for the three metal/metal interfaces. As the electronic DMM is based on the electron flux in the metals, the fact that the conductance across various metal/metal interfaces can be well predicted by simple considerations of the electronic DMM could

lead to the engineering of interfaces with tailored  $h_{ee}$  designed by simplistic arguments based on electronic flux and the electronic heat capacity of the metals comprising the interface.

Although the energy exchange at metal/metal interfaces appears simplistic from an analytical perspective, the picture of energy transfer at a metal/nonmetal interfaces becomes convoluted by the addition of different energy pathways. As proposed by Majumdar and Reddy,<sup>[192]</sup> the possible pathways for heat conduction that can occur at metal/nonmetal interfaces are shown in **Figure 13a**. These pathways are i) metal electron–metal phonon coupling at the metal/nonmetal interface ( $h_{e-mp}$ ), ii) phonon–phonon coupling across the interface ( $h_{p-p}$ ), and iii) metal electron–nonmetal phonon coupling directly across the interface ( $h_{e-nmp}$ ). At a metal/nonmetal interface, electronic contributions to interfacial conductance have been mostly suggested to be nonexistent under equilibrium conditions.<sup>[19,34,63,70,71,193,194]</sup> The interest in this topic was triggered by the seminal work from Stoner and Maris where they reported measurements of  $h_K$  between a series of metals and nonmetals to which they compared with various phonon–phonon interface models and found discrepancies between theory and experiments.<sup>[30]</sup> This led Huberman and Overhauser, Sergeev, and more recently Mahan to propose theoretical models of  $h_{e-nmp}$  channel to explain the experimental results.<sup>[195–198]</sup>

Since Stoner and Maris' experimental results, Lyeo and Cahill have shown that Pb and Bi, which have similar phonon spectrums yet different electronic densities around their

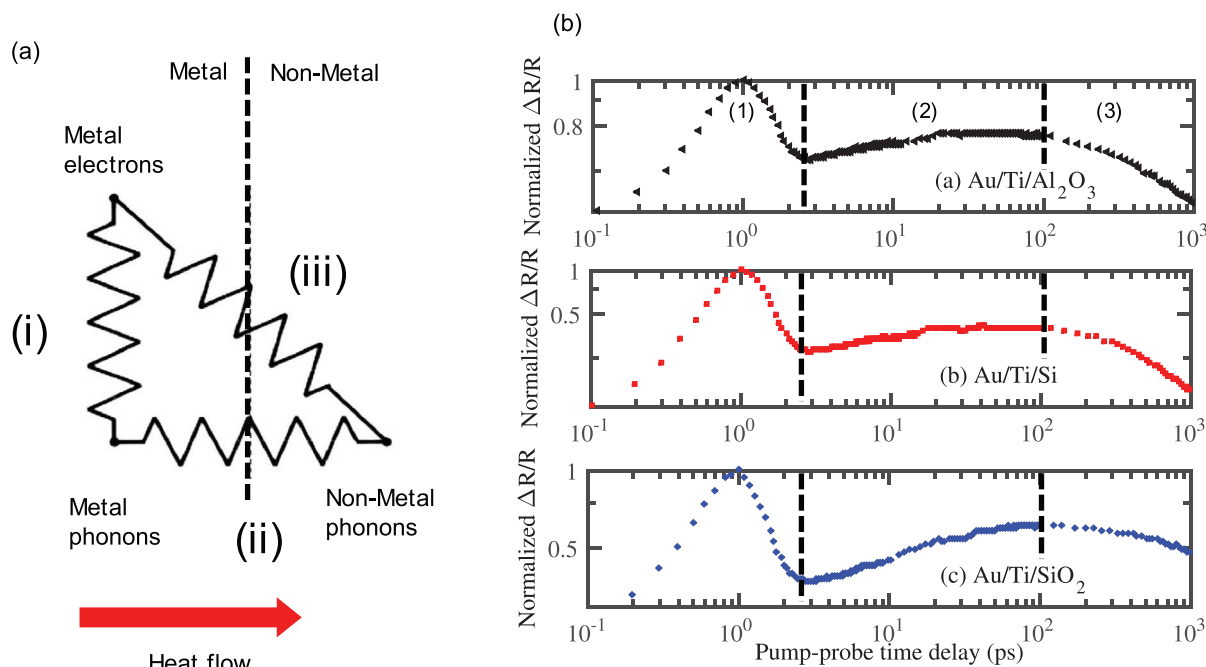


**Figure 13.** a) Schematic representation of pathways for interfacial heat flow for a metal/nonmetal interface. The electron–phonon coupling in the bulk of the metal presents a resistance in series with the phonon–phonon coupling across the interface. Electrons can also directly transfer their energy across the interface to the phonons on the nonmetal side. b) TDTR data taken from Giri et al.<sup>[70]</sup> showing the response of 40 nm Au deposited on various substrates with a thin Ti adhesion layer. The TDTR signal decays rapidly for the first few picoseconds after laser pulse absorption due to electronic relaxation in the metal. This is followed by a slow rise in the TDTR signal that is attributed to the heat flow from the Ti layer to the Au layer as most of the laser energy is first deposited in the Ti layer with the relatively higher electron–phonon coupling factor. The longer time regime corresponds to the heat flow across the interface and the diffusion of energy into the substrate.



respective Fermi surfaces, have similar  $h_K$  across the diamond interfaces. Their results suggest that  $h_{e-nmp}$  is not a viable channel for heat conductance across metal/nonmetal interfaces. This is also supported by results from Hohensee et al.<sup>[19]</sup> where they also studied interfacial conductance for different metals with vastly different electronic DOS near the Fermi energy on diamond substrates and concluded that electron–phonon interaction at the interface does not affect  $h_K$  across metal/diamond interfaces. However, recent theoretical works based on the two-temperature model<sup>[199–202]</sup> have suggested that strong electron–phonon coupling in the metal can lead to an increase in the phonon–phonon thermal conductance, while for weak electron–phonon coupling in the metal, this resistive pathway could become significant.<sup>[193,203]</sup> There have also been several experimental works that have argued that under time scales where there is strong nonequilibrium between electrons and phonons in the metal,  $h_{e-vmp}$  could potentially increase the rate of energy exchange at the interface.<sup>[70,204–206]</sup> For example, Giri et al.<sup>[70]</sup> studied electron and phonon thermal coupling mechanisms at interfaces between gold films with and without Ti adhesion layers on various substrates via pump–probe technique. The fact that the Ti layer has a stronger electron–phonon coupling compared to the Au layer combined with the fact that the Au layers in their study are thinner than the ballistic mean-free path of electrons, it can be shown that most of the laser energy is deposited in the thin Ti layer initially in the time period labeled (1) in Figure 13b. By considering the results for different substrates and varying laser fluences, they argue that only in this early time period does electron–interface scattering affect energy transport. However, for longer delay times in the 100 ps to nanosecond regime labeled as (2) in Figure 13b, electron–interface scattering is shown to have negligible influence on the thermal boundary conductances between the Au/Ti and the substrates. Note, at these longer time scales the electrons and phonons in the metal have equilibrated, which is also characterized by the thermalization of the Au film in the regime labeled (2) where the energy deposited by the electrons in the Ti layer equilibrates with the colder Au lattice, which results in the increase in the thermoreflectance signal at these time periods due to the heating of the Au layer.

In contrast to the results presented in the above paragraph, Sadasivam et al.<sup>[95]</sup> studied titanium silicide (metal)/silicon (nonmetal) interface via ab initio approaches to show that the strength of electron–phonon and phonon–phonon heat transfer across the interface can be on the same order of magnitude. In their work, the electron and phonon dispersion relations of  $\text{TiSi}_2$  and the  $\text{TiSi}_2/\text{Si}$  interface were obtained using first-principles calculations without any adjustable parameters. They computed the Eliashberg function that quantifies the coupling between electrons and phonons.<sup>[200,207,208]</sup> Their results are summarized in Figure 14, which shows the contributions from the three channels of energy transfer (as discussed above) across the  $\text{TiSi}_2/\text{Si}$  interface. Their results show that the coupling strength of electrons with phonon modes in the nonmetal ( $h_{e-vmp}$ ) is of the same order of magnitude as the coupling of electrons to phonon modes in the bulk of  $\text{TiSi}_2$  ( $h_{e-mp}$ ). As shown in Figure 14,  $h_{e-vmp}$  contributions are also comparable to the phonon–phonon conductance across the interface

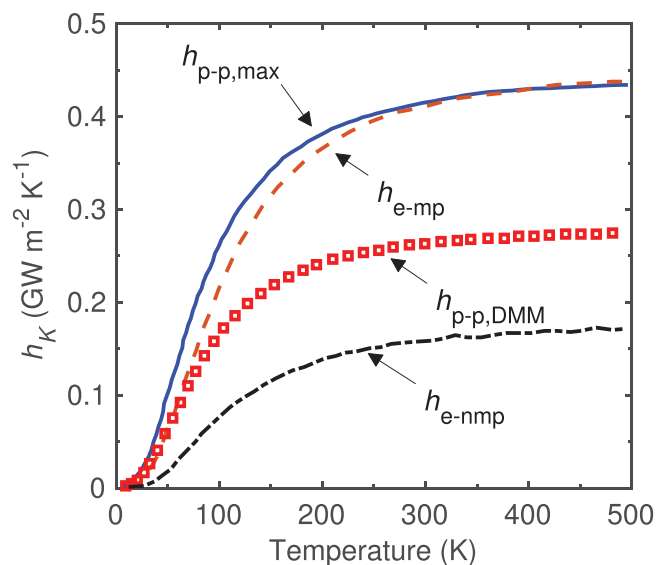


**Figure 14.** Thermal conductance due to the various channels of heat flow for a  $\text{TiSi}_2/\text{Si}$  system as adapted from Sadasivam et al.<sup>[95]</sup> The conductance due to the direct coupling of the electrons to the phonons in the nonmetal ( $h_{e-vmp}$ ) is in the same order of magnitude as the conductance due to phonon–phonon coupling across the interface from the metal to the nonmetal ( $h_{p-p}$ ).

predicted via DMM in the harmonic approximation. Their ab initio based calculations show that electron–phonon interaction across an interface could present a parallel pathway to phonon–phonon coupling for heat conduction across metal/nonmetal interfaces, contrary to commonly adopted models where  $h_{e-vmp}$  is considered to have a negligible effect on the total  $h_K$ .<sup>[71,192,209]</sup>

## 11. Conclusion

The comprehensive understanding of thermal boundary conductance across nanoscale interfaces with an accurate description of the scattering mechanisms of the fundamental energy carriers is critical to current as well as emerging technologies. The fundamental processes driving electron and phonon interactions at interfaces have been difficult to accurately predict with simplified theoretical models, shrouding the complete understanding of these fundamental processes. However, major advances in computational tools such as molecular dynamics simulations and parameter-free first-principles calculations have paved the way for an exact description of the dynamical processes occurring at and near nanoscale interfaces, making it feasible to fully understand and control these processes to tune thermal boundary conductance. A growing body of work based on molecular dynamics simulations have been able to predict interfacial heat transport by including spectral and mode-level details of the vibrational energy carriers. Atomic Green's function methods, wave packet simulations, and harmonic lattice dynamics calculations have aided in the further understanding of interfacial transport, albeit with various approximations that are avoided with molecular dynamics simulations or fully first-principles calculations. Modal and

spectral decomposition techniques to study the energy transport pathways across interfacial regions at heteromaterial junctions offer the unique opportunity to gain insight into specific mode conversion that can occur near an interface and provide a deeper level of understanding. Therefore, further refinements in the interatomic interactions in molecular dynamics simulations, which can correctly capture the interfacial chemistry such as the bonding environment and defects around the interface for a comprehensive set of material systems would be a significant stride towards a more complete understanding of thermal boundary conductance. Similarly, a theoretical framework to support first-principles calculations that can incorporate both electron and phonon dynamics at interfaces would also be a significant achievement from the computational side.

From the experimental side, metrologies based on pump-probe techniques such as time-domain thermorefectance and time-resolved magneto-optic Kerr-effect thermometry have already shaped major advances and hold the potential for further progress in understanding interfacial heat flow. The ability to perform more detailed measurements of the spectral contribution of various modes to thermal boundary conductance will be an important development moving forward. Further refinements and advances in these types of techniques could also lead to in situ characterization of heat transfer in nanoscale devices carried out at their operating conditions. Along with the thermal characterization metrologies, the ability to control growth processes with atomic resolution has also led to the realization of “more model” interfaces that have allowed for the critical assessment and validation of various theoretical models. However, there are only a handful of these studies on limited material systems that have investigated the heat transfer across epitaxially grown interfaces,<sup>[24,25,27,33,210]</sup> leaving a considerable void to be filled with future work on these types of interfaces formed between various material systems with different energy carriers dictating heat flow across interfaces.

## Acknowledgements

This work was supported under a MURI program through the Office of Naval Research, Grant No. N00014-18-1-2429.

## Conflict of Interest

The authors declare no conflict of interest.

## Keywords

interfacial modes, Kapitza resistance, thermal boundary conductance, thermal conductivity

Received: May 14, 2019

Revised: July 16, 2019

Published online: August 16, 2019

- [1] D. G. Cahill, W. K. Ford, K. E. Goodson, G. D. Mahan, A. Majumdar, H. J. Maris, R. Merlin, S. R. Phillpot, *J. Appl. Phys.* **2003**, 93, 793.

- [2] D. G. Cahill, P. V. Braun, G. Chen, D. R. Clarke, S. Fan, K. E. Goodson, P. Keblinski, W. P. King, G. D. Mahan, A. Majumdar, H. J. Maris, S. R. Phillpot, E. Pop, L. Shi, *Appl. Phys. Rev.* **2014**, 1, 011305.
- [3] Y. Shen, J. Gaskins, X. Xie, B. M. Foley, R. Cheaito, P. E. Hopkins, J. C. Campbell, *J. Lightwave Technol.* **2017**, 35, 4242.
- [4] Q. Zhou, A. Cross, Y. Fu, A. Beling, B. Foley, P. Hopkins, J. Campbell, *IEEE Photonics J.* **2013**, 5, 6800307.
- [5] E. Pop, *Nano Res.* **2010**, 3, 147.
- [6] B. S. Williams, *Nat. Photonics* **2007**, 1, 517.
- [7] H.-S. P. Wong, S. Raoux, S. Kim, J. Liang, J. P. Reifenberg, B. Rajendran, M. Asheghi, K. E. Goodson, *Proc. IEEE* **2010**, 98, 2201.
- [8] E. A. Scott, J. T. Gaskins, S. W. King, P. E. Hopkins, *APL Mater.* **2018**, 6, 058302.
- [9] J. Gaskins, P. E. Hopkins, D. R. Merrill, S. Bauers, E. Hadland, D. Johnson, D. Koh, J. h. Yum, S. Banerjee, B. Nordell, M. M. Paquette, A. N. Caruso, W. Lanford, P. Henry, L. Ross, H. Li, L. Li, M. French, A. M. Rudolph, S. King, *ECS J. Solid State Sci. Technol.* **2017**, 6, N189.
- [10] R. M. Costescu, D. G. Cahill, F. H. Fabreguette, Z. A. Sechrist, S. M. George, *Science* **2004**, 303, 989.
- [11] M. D. Losego, I. P. Blitz, R. A. Vaia, D. G. Cahill, P. V. Braun, *Nano Lett.* **2013**, 13, 2215.
- [12] A. Giri, B. F. Donovan, P. E. Hopkins, *Phys. Rev. Mater.* **2018**, 2, 056002.
- [13] H. Ji, D. P. Sellan, M. T. Pettes, X. Kong, J. Ji, L. Shi, R. S. Ruoff, *Energy Environ. Sci.* **2014**, 7, 1185.
- [14] S. Merabia, S. Shenogin, L. Joly, P. Keblinski, J.-L. Barrat, *Proc. Natl. Acad. Sci. USA* **2009**, 106, 15113.
- [15] L. R. Hirsch, R. J. Stafford, J. A. Bankson, S. R. Serfshen, B. Rivera, R. E. Price, J. D. Hazle, N. J. Halas, J. L. West, *Proc. Natl. Acad. Sci. USA* **2003**, 100, 13549.
- [16] P. L. Kapitza, *J. Electrochem. Plat. Technol.* **1941**, 11, 1.
- [17] J. Kimling, A. Philippi-Kobs, J. Jacobsohn, H. P. Oepen, D. G. Cahill, *Phys. Rev. B* **2017**, 95, 184305.
- [18] S. W. Fong, A. Sood, L. Chen, N. Kumari, M. Asheghi, K. E. Goodson, G. A. Gibson, H.-S. P. Wong, *J. Appl. Phys.* **2016**, 120, 015103.
- [19] G. T. Hohensee, R. B. Wilson, D. G. Cahill, *Nat. Commun.* **2015**, 6, 6578.
- [20] X. Qian, P. Jiang, R. Yang, *Mater. Today Phys.* **2017**, 3, 70.
- [21] B. F. Donovan, C. J. Szejewski, J. C. Duda, R. Cheaito, J. T. Gaskins, C.-Y. P. Yang, C. Constantin, R. E. Jones, P. E. Hopkins, *Appl. Phys. Lett.* **2014**, 105, 203502.
- [22] R. B. Wilson, D. G. Cahill, *Nat Commun.* **2014**, 5, 5075.
- [23] E. Ziade, J. Yang, G. Brummer, D. Nothern, T. Moustakas, A. J. Schmidt, *Appl. Phys. Lett.* **2015**, 107, 091605.
- [24] R. M. Costescu, M. A. Wall, D. G. Cahill, *Phys. Rev. B* **2003**, 67, 054302.
- [25] R. B. Wilson, B. A. Apgar, W.-P. Hsieh, L. W. Martin, D. G. Cahill, *Phys. Rev. B* **2015**, 91, 115414.
- [26] P. E. Hopkins, R. J. Stevens, P. M. Norris, *J. Heat Transfer* **2008**, 130, 022401.
- [27] J. T. Gaskins, G. Kotsonis, A. Giri, S. Ju, A. Rohskopf, Y. Wang, T. Bai, E. Sachet, C. T. Shelton, Z. Liu, Z. Cheng, B. M. Foley, S. Graham, T. Luo, A. Henry, M. S. Goorsky, J. Shiomi, J.-P. Maria, P. E. Hopkins, *Nano Lett.* **2018**, 18, 7469.
- [28] A. Giri, J.-P. Niemela, T. Tynell, J. T. Gaskins, B. F. Donovan, M. Karppinen, P. E. Hopkins, *Phys. Rev. B* **2016**, 93, 115310.
- [29] D. P. Schroeder, Z. Aksamija, A. Rath, P. M. Voyles, M. G. Lagally, M. A. Eriksson, *Phys. Rev. Lett.* **2015**, 115, 256101.
- [30] R. J. Stoner, H. J. Maris, T. R. Anthony, W. F. Banholzer, *Phys. Rev. Lett.* **1992**, 68, 1563.

- [31] R. Cheaito, J. T. Gaskins, M. E. Caplan, B. F. Donovan, B. M. Foley, A. Giri, J. C. Duda, C. J. Szejewski, C. Constantin, H. J. Brown-Shaklee, J. F. Ihlefeld, P. E. Hopkins, *Phys. Rev. B* **2015**, 91, 035432.
- [32] R. J. Stevens, A. N. Smith, P. M. Norris, *J. Heat Transfer* **2005**, 127, 315.
- [33] N. Ye, J. P. Feser, S. Sadasivam, T. S. Fisher, T. Wang, C. Ni, A. Janotti, *Phys. Rev. B* **2017**, 95, 085430.
- [34] H.-K. Lyoo, D. G. Cahill, *Phys. Rev. B* **2006**, 73, 144301.
- [35] A. Giri, S. W. King, W. A. Lanford, A. B. Mei, D. Merrill, L. Li, R. Oviedo, J. Richards, D. H. Olson, J. L. Braun, J. T. Gaskins, F. Deangelis, A. Henry, P. E. Hopkins, *Adv. Mater.* **2018**, 30, 1804097.
- [36] R. Cheaito, K. Hattar, J. T. Gaskins, A. K. Yadav, J. C. Duda, T. E. Beechem, J. F. Ihlefeld, E. S. Piekos, J. K. Baldwin, A. Misra, P. E. Hopkins, *Appl. Phys. Lett.* **2015**, 106, 093114.
- [37] B. C. Gendrum, D. G. Cahill, R. S. Averback, *Phys. Rev. B* **2005**, 72, 245426.
- [38] R. B. Wilson, D. G. Cahill, *Phys. Rev. Lett.* **2012**, 108, 255901.
- [39] P. E. Hopkins, *ISRN Mech. Eng.* **2013**, 2013, 682586.
- [40] C. Monachon, L. Weber, C. Dames, *Annu. Rev. Mater. Res.* **2016**, 46, 433.
- [41] G. Chen, *Nanoscale Energy Transport and Conversion: A Parallel Treatment of Electrons, Molecules, Phonons, and Photons*, Oxford University Press, USA **2005**.
- [42] J. C. Duda, P. E. Hopkins, J. L. Smoyer, M. L. Bauer, T. S. English, C. B. Saltonstall, P. M. Norris, *Nanoscale Microscale Thermophys. Eng.* **2010**, 14, 21.
- [43] C. Hua, X. Chen, N. K. Ravichandran, A. J. Minnich, *Phys. Rev. B* **2017**, 95, 205423.
- [44] E. T. Swartz, R. O. Pohl, *Rev. Mod. Phys.* **1989**, 61, 605.
- [45] W. A. Little, *Can. J. Phys.* **1959**, 37, 334.
- [46] I. M. Khalatnikov, *J. Exp. Theor. Phys.* **1952**, 22, 687.
- [47] P. Reddy, K. Castelino, A. Majumdar, *Appl. Phys. Lett.* **2005**, 87, 211908.
- [48] R. Prasher, *Appl. Phys. Lett.* **2009**, 94, 041905.
- [49] P. E. Hopkins, J. C. Duda, P. M. Norris, *J. Heat Transfer* **2011**, 133, 062401.
- [50] J. C. Duda, J. L. Smoyer, P. M. Norris, P. E. Hopkins, *Appl. Phys. Lett.* **2009**, 95, 031912.
- [51] P. E. Hopkins, P. M. Norris, *J. Heat Transfer* **2009**, 131, 022402.
- [52] P. E. Hopkins, T. Beechem, J. C. Duda, K. Hattar, J. F. Ihlefeld, M. A. Rodriguez, E. S. Piekos, *Phys. Rev. B* **2011**, 84, 125408.
- [53] J. C. Duda, P. M. Norris, P. E. Hopkins, *J. Heat Transfer* **2011**, 133, 074501.
- [54] P. E. Hopkins, P. M. Norris, *Nanoscale Microscale Thermophys. Eng.* **2007**, 11, 247.
- [55] P. E. Hopkins, *J. Appl. Phys.* **2009**, 106, 013528.
- [56] G. Slack, *J. Phys. Chem. Solids* **1973**, 34, 321.
- [57] K. Gordiz, A. Henry, *Sci. Rep.* **2016**, 6, 23139.
- [58] K. Gordiz, A. Henry, *J. Appl. Phys.* **2016**, 119, 015101.
- [59] O. L. Krivanek, T. C. Lovejoy, N. Dellby, T. Aoki, R. W. Carpenter, P. Rez, E. Soignard, J. Zhu, P. E. Batson, M. J. Lagos, R. F. Egerton, P. A. Crozier, *Nature* **2014**, 514, 209.
- [60] T. Murakami, T. Hori, T. Shiga, J. Shiomi, *Appl. Phys. Express* **2014**, 7, 121801.
- [61] A. Giri, P. E. Hopkins, *Sci. Rep.* **2017**, 7, 11011.
- [62] E. Dechaumphai, D. Lu, J. J. Kan, J. Moon, E. E. Fullerton, Z. Liu, R. Chen, *Nano Lett.* **2014**, 14, 2448.
- [63] X. Li, W. Park, Y. P. Chen, X. Ruan, *Appl. Phys. Lett.* **2017**, 111, 143102.
- [64] T. Beechem, P. E. Hopkins, *J. Appl. Phys.* **2009**, 106, 124301.
- [65] P. E. Hopkins, P. M. Norris, R. J. Stevens, T. E. Beechem, S. Graham, *J. Heat Transfer* **2008**, 130, 062402.
- [66] P. E. Hopkins, L. M. Phinney, J. R. Serrano, T. E. Beechem, *Phys. Rev. B* **2010**, 82, 085307.
- [67] P. E. Hopkins, J. C. Duda, C. W. Petz, J. A. Floro, *Phys. Rev. B* **2011**, 84, 035438.
- [68] J. C. Duda, P. E. Hopkins, *Appl. Phys. Lett.* **2012**, 100, 111602.
- [69] R. J. Stoner, H. J. Maris, *Phys. Rev. B* **1993**, 48, 16373.
- [70] A. Giri, J. T. Gaskins, B. F. Donovan, C. Szejewski, R. J. Warzoha, M. A. Rodriguez, J. Ihlefeld, P. E. Hopkins, *J. Appl. Phys.* **2015**, 117, 105105.
- [71] P. Singh, M. Seong, S. Sinha, *Appl. Phys. Lett.* **2013**, 102, 181906.
- [72] M. A. Panzer, H. M. Duong, J. Okawa, J. Shiomi, B. L. Wardle, S. Maruyama, K. E. Goodson, *Nano Lett.* **2010**, 10, 2395.
- [73] K. Sääskilähti, J. Oksanen, J. Tulkki, S. Volz, *Phys. Rev.* **2014**, B 90, 134312.
- [74] X. Wu, T. Luo, *J. Appl. Phys.* **2014**, 115, 014901.
- [75] D. A. Young, H. J. Maris, *Phys. Rev. B* **1989**, 40, 3685.
- [76] H. Zhao, J. B. Freund, *J. Appl. Phys.* **2005**, 97, 024903.
- [77] P. K. Schelling, S. R. Phillpot, P. Keblinski, *Appl. Phys. Lett.* **2002**, 80, 2484.
- [78] X. W. Zhou, R. E. Jones, C. J. Kimmer, J. C. Duda, P. E. Hopkins, *Phys. Rev. B* **2013**, 87, 094303.
- [79] N. A. Roberts, D. G. Walker, *J. Appl. Phys.* **2010**, 108, 123515.
- [80] C. Kimmer, S. Aubry, A. Skye, P. K. Schelling, *Phys. Rev. B* **2007**, 75, 144105.
- [81] J. C. Duda, C. J. Kimmer, W. A. Soffa, X. W. Zhou, R. E. Jones, P. E. Hopkins, *J. Appl. Phys.* **2012**, 112, 093515.
- [82] P. E. Hopkins, P. M. Norris, M. S. Tsegaye, A. W. Ghosh, *J. Appl. Phys.* **2009**, 106, 063503.
- [83] C. B. Saltonstall, C. A. Polanco, J. C. Duda, A. W. Ghosh, P. M. Norris, P. E. Hopkins, *J. Appl. Phys.* **2013**, 113, 013516.
- [84] S. Sadasivam, Y. Che, Z. Huang, L. Chen, S. Kumar, T. S. Fisher, *Annu. Rev. Heat Transfer* **2014**, 17, 89.
- [85] Z.-Y. Ong, G. Zhang, *Phys. Rev. B* **2015**, 91, 174302.
- [86] B. Latour, N. Shulumba, A. J. Minnich, *Phys. Rev. B* **2017**, 96, 104310.
- [87] N. Mingo, L. Yang, *Phys. Rev. B* **2003**, 68, 245406.
- [88] Y. Lu, J. Guo, *Appl. Phys. Lett.* **2012**, 101, 043112.
- [89] A. Y. Serov, Z.-Y. Ong, E. Pop, *Appl. Phys. Lett.* **2013**, 102, 033104.
- [90] Z. Tian, K. Esfarjani, G. Chen, *Phys. Rev. B* **2012**, 86, 235304.
- [91] W. Zhang, T. S. Fisher, N. Mingo, *J. Heat Transfer* **2006**, 129, 483.
- [92] Y. Cai, J. Lan, G. Zhang, Y.-W. Zhang, *Phys. Rev. B* **2014**, 89, 035438.
- [93] Z.-Y. Ong, Y. Cai, G. Zhang, Y.-W. Zhang, *J. Phys. Chem. C* **2014**, 118, 25272.
- [94] P. Scuracchio, S. Costamagna, F. M. Peeters, A. Dobry, *Phys. Rev. B* **2014**, 90, 035429.
- [95] S. Sadasivam, U. V. Waghmare, T. S. Fisher, *J. Appl. Phys.* **2015**, 117, 134502.
- [96] X. Zhou, J. Jankowska, L. Li, A. Giri, P. E. Hopkins, O. V. Prezhdo, *ACS Appl. Mater. Interfaces* **2017**, 9, 43343.
- [97] S. Sadasivam, N. Ye, J. P. Feser, J. Charles, K. Miao, T. Kubis, T. S. Fisher, *Phys. Rev. B* **2017**, 95, 085310.
- [98] C. A. Polanco, L. Lindsay, *Phys. Rev. B* **2019**, 99, 075202.
- [99] J. Zhang, C. A. Polanco, A. W. Ghosh, *J. Heat Transfer* **2018**, 140, 092405.
- [100] M. P. Allen, D. J. Tildesley, *Computer Simulation of Liquids*, Clarendon Press, NY, USA **1989**.
- [101] J.-L. Barrat, F. Chiaruttini, *Mol. Phys.* **2003**, 101, 1605.
- [102] Y. Chalopin, K. Esfarjani, A. Henry, S. Volz, G. Chen, *Phys. Rev. B* **2012**, 85, 195302.
- [103] R. J. Stevens, L. V. Zhigilei, P. M. Norris, *Int. J. Heat Mass Transfer* **2007**, 50, 3977.
- [104] E. S. Landry, A. J. H. McGaughey, *Phys. Rev. B* **2009**, 80, 165304.
- [105] P. K. Schelling, S. R. Phillpot, P. Keblinski, *Phys. Rev. B* **2002**, 65, 144306.
- [106] Y. Chalopin, S. Volz, *Appl. Phys. Lett.* **2013**, 103, 051602.
- [107] K. Gordiz, A. Henry, *New J. Phys.* **2015**, 17, 103002.

- [108] W. Lv, A. Henry, *New J. Phys.* **2016**, *18*, 013028.
- [109] T. Feng, W. Yao, Z. Wang, J. Shi, C. Li, B. Cao, X. Ruan, *Phys. Rev. B* **2017**, *95*, 195202.
- [110] A. Giri, J. L. Braun, P. E. Hopkins, *J. Phys. Chem. C* **2016**, *120*, 24847.
- [111] T. Feng, Y. Zhong, J. Shi, X. Ruan, *Phys. Rev. B* **2019**, *99*, 045301.
- [112] B. Ramos-Alvarado, S. Kumar, *J. Phys. Chem. C* **2017**, *121*, 11380.
- [113] J. Tersoff, *Phys. Rev. B* **1989**, *39*, 5566.
- [114] J. Tersoff, *Phys. Rev. B* **1988**, *37*, 6991.
- [115] L. Lindsay, D. A. Broido, *Phys. Rev. B* **2010**, *81*, 205441.
- [116] G. Joshi, H. Lee, Y. Lan, X. Wang, G. Zhu, D. Wang, R. W. Gould, D. C. Cuff, M. Y. Tang, M. S. Dresselhaus, G. Chen, Z. Ren, *Nano Lett.* **2008**, *8*, 4670.
- [117] F. H. Stillinger, T. A. Weber, *Phys. Rev. B* **1985**, *31*, 5262.
- [118] Y. Chalopin, N. Mingo, J. Diao, D. Srivastava, S. Volz, *Appl. Phys. Lett.* **2012**, *101*, 221903.
- [119] G. Domingues, S. Volz, K. Joulain, J.-J. Greffet, *Phys. Rev. Lett.* **2005**, *94*, 085901.
- [120] Z.-Y. Ong, E. Pop, *J. Appl. Phys.* **2010**, *108*, 103502.
- [121] R. J. Hardy, *Phys. Rev.* **1963**, *132*, 168.
- [122] K. Sääskilahti, J. Oksanen, R. P. Linna, J. Tulkki, *Phys. Rev. E* **2012**, *86*, 031107.
- [123] Y. Zhou, M. Hu, *Phys. Rev. B* **2017**, *95*, 115313.
- [124] K. Gordiz, A. Henry, *Appl. Phys. Lett.* **2016**, *108*, 181606.
- [125] J. C. Duda, P. E. Hopkins, T. E. Beechem, J. L. Smoyer, P. M. Norris, *Superlattices Microstruct.* **2010**, *47*, 550.
- [126] J. C. Duda, T. S. English, E. S. Piekos, W. A. Soffa, L. V. Zhigilei, P. E. Hopkins, *Phys. Rev. B* **2011**, *84*, 193301.
- [127] A. Giri, P. E. Hopkins, J. G. Wessel, J. C. Duda, *J. Appl. Phys.* **2015**, *118*, 165303.
- [128] F. Jolly, F. Rochet, G. Dufour, C. Grupp, A. Taleb-Ibrahimi, *J. Non-Cryst. Solids* **2001**, *280*, 150.
- [129] P. B. Allen, J. L. Feldman, J. Fabian, F. Wooten, *Philos. Mag. B* **1999**, *79*, 1715.
- [130] J. L. Feldman, M. D. Kluge, P. B. Allen, F. Wooten, *Phys. Rev. B* **1993**, *48*, 12589.
- [131] J. M. Larkin, A. J. H. McGaughey, *Phys. Rev. B* **2014**, *89*, 144303.
- [132] J. A. Tomko, D. H. Olson, A. Giri, J. T. Gaskins, B. F. Donovan, S. M. OâMalley, P. E. Hopkins, *Langmuir* **2019**, *35*, 2106.
- [133] K. Gordiz, A. Henry, *J. Appl. Phys.* **2017**, *121*, 025102.
- [134] D. Hondongwa, L. Olasov, B. Daly, S. King, J. Bielefeld, *Thin Solid Films* **2011**, *519*, 7895.
- [135] J. Chen, S. W. King, E. Muthuswamy, A. Koryttseva, D. Wu, A. Navrotsky, *J. Am. Ceram. Soc.* **2016**, *99*, 2752.
- [136] K. Gordiz, M. G. Muraleedharan, A. Henry, *J. Appl. Phys.* **2019**, *125*, 135102.
- [137] T. S. English, J. C. Duda, J. L. Smoyer, D. A. Jordan, P. M. Norris, L. V. Zhigilei, *Phys. Rev. B* **2012**, *85*, 035438.
- [138] J. P. Freedman, X. Yu, R. F. Davis, A. J. Gellman, J. A. Malen, *Phys. Rev. B* **2016**, *93*, 035309.
- [139] W. Park, A. Sood, J. Park, M. Asheghi, R. Sinclair, K. E. Goodson, *Nanoscale Microscale Thermophys. Eng.* **2017**, *21*, 134.
- [140] E. Lee, T. Zhang, T. Yoo, Z. Guo, T. Luo, *ACS Appl. Mater. Interfaces* **2016**, *8*, 35505.
- [141] E. Lee, T. Zhang, M. Hu, T. Luo, *Phys. Chem. Chem. Phys.* **2016**, *18*, 16794.
- [142] C. S. Gorham, K. Hattar, R. Cheaito, J. C. Duda, J. T. Gaskins, T. E. Beechem, J. F. Ihlefeld, L. B. Biedermann, E. S. Piekos, D. L. Medlin, P. E. Hopkins, *Phys. Rev. B* **2014**, *90*, 024301.
- [143] Z. Ge, D. G. Cahill, P. V. Braun, *Phys. Rev. Lett.* **2006**, *96*, 186101.
- [144] H. Harikrishna, W. A. Ducker, S. T. Huxtable, *Appl. Phys. Lett.* **2013**, *102*, 251606.
- [145] A. Giri, P. E. Hopkins, *Appl. Phys. Lett.* **2014**, *105*, 033106.
- [146] S. Shenogin, A. Bodapati, P. Keblinski, A. J. H. McGaughey, *J. Appl. Phys.* **2009**, *105*, 034906.
- [147] Y. Wang, P. Keblinski, *Appl. Phys. Lett.* **2011**, *99*, 073112.
- [148] K. Sääskilahti, J. Oksanen, J. Tulkki, S. Volz, *Phys. Rev. E* **2016**, *93*, 052141.
- [149] D. Huang, R. Ma, T. Zhang, T. Luo, *ACS Appl. Mater. Interfaces* **2018**, *10*, 28159.
- [150] M. D. Losego, M. E. Grady, N. R. Sottos, D. G. Cahill, P. V. Braun, *Nat. Mater.* **2012**, *11*, 502.
- [151] S. Majumdar, J. A. Sierra-Suarez, S. N. Schiffres, W.-L. Ong, I. C. Fred Higgs, A. J. H. McGaughey, J. A. Malen, *Nano Lett.* **2015**, *15*, 2985.
- [152] M. Hu, X. Zhang, D. Poulikakos, C. P. Grigoropoulos, *Int. J. Heat Mass Transfer* **2011**, *54*, 5183.
- [153] C. A. Polanco, R. Rastgarkafshgarkolaei, J. Zhang, N. Q. Le, P. M. Norris, A. W. Ghosh, *Phys. Rev. B* **2017**, *95*, 195303.
- [154] R. Rastgarkafshgarkolaei, J. Zhang, C. A. Polanco, N. Q. Le, A. W. Ghosh, P. M. Norris, *Nanoscale* **2019**, *11*, 6254.
- [155] A. Giri, J. L. Braun, P. E. Hopkins, *J. Appl. Phys.* **2016**, *119*, 235305.
- [156] K. R. Hahn, M. Puligheddu, L. Colombo, *Phys. Rev. B* **2015**, *91*, 195313.
- [157] S. Walton, B. Foley, S. Hernández, D. Boris, M. Baraket, J. Duda, J. Robinson, P. Hopkins, *Surf. Coat. Technol.* **2017**, *314*, 148.
- [158] P. E. Hopkins, M. Baraket, E. V. Barnat, T. E. Beechem, S. P. Kearney, J. C. Duda, J. T. Robinson, S. G. Walton, *Nano Lett.* **2012**, *12*, 590.
- [159] S. G. Walton, B. M. Foley, J. Tomko, D. R. Boris, E. D. Gillman, S. C. Hernández, A. Giri, T. B. Petrova, P. E. Hopkins, *J. Appl. Phys.* **2018**, *124*, 043301.
- [160] B. M. Foley, S. C. Hernandez, J. C. Duda, J. T. Robinson, S. G. Walton, P. E. Hopkins, *Nano Lett.* **2015**, *15*, 4876.
- [161] Y. K. Koh, M.-H. Bae, D. G. Cahill, E. Pop, *Nano Lett.* **2010**, *10*, 4363.
- [162] K. M. Freedy, A. Giri, B. M. Foley, M. R. Barone, P. E. Hopkins, S. McDonnell, *Nanotechnology* **2018**, *29*, 145201.
- [163] D. H. Olson, K. M. Freedy, S. J. McDonnell, P. E. Hopkins, *Appl. Phys. Lett.* **2018**, *112*, 171602.
- [164] E. Yalon, A. B. Aslan, K. K. H. Smithe, C. J. McClellan, S. V. Suryavanshi, F. Xiong, A. Sood, C. M. Neumann, X. Xu, K. E. Goodson, T. F. Heinz, E. Pop, *ACS Appl. Mater. Interfaces* **2017**, *9*, 43013.
- [165] A. Behranginia, Z. Hemmat, A. K. Majee, C. J. Foss, P. Yasaei, Z. Aksamija, A. Salehi-Khojin, *ACS Appl. Mater. Interfaces* **2018**, *10*, 24892.
- [166] E. Yalon, C. J. McClellan, K. K. H. Smithe, M. M. Rojo, R. L. Xu, S. V. Suryavanshi, A. J. Gabourie, C. M. Neumann, F. Xiong, A. B. Farimani, E. Pop, *Nano Lett.* **2017**, *17*, 3429.
- [167] Z. Chen, W. Jang, W. Bao, C. N. Lau, C. Dames, *Appl. Phys. Lett.* **2009**, *95*, 161910.
- [168] X. Li, Y. Yan, L. Dong, J. Guo, A. Aiyiti, X. Xu, B. Li, *J. Phys. D: Appl. Phys.* **2017**, *50*, 104002.
- [169] P. Yasaei, C. J. Foss, K. Karis, A. Behranginia, A. I. El-Ghannour, A. Fathizadeh, J. Olivares, A. K. Majee, C. D. Foster, F. Khalili-Araghi, Z. Aksamija, A. Salehi-Khojin, *Adv. Mater. Interfaces* **2017**, *4*, 1700334.
- [170] P. Yasaei, Z. Hemmat, C. J. Foss, S. J. Li, L. Hong, A. Behranginia, L. Majidi, R. F. Klie, M. W. Barsoum, Z. Aksamija, A. Salehi-Khojin, *Adv. Mater.* **2018**, *30*, 1801629.
- [171] P. Yasaei, A. Behranginia, Z. Hemmat, A. I. El-Ghannour, C. D. Foster, A. Salehi-Khojin, *2D Mater.* **2017**, *4*, 035027.
- [172] J. Yang, E. Ziade, C. Maragliano, R. Crowder, X. Wang, M. Stefancich, M. Chiesa, A. K. Swan, A. J. Schmidt, *J. Appl. Phys.* **2014**, *116*, 023515.
- [173] Z.-Y. Ong, Y. Cai, G. Zhang, *Phys. Rev. B* **2016**, *94*, 165427.
- [174] Z.-Y. Ong, B. Qiu, S. Xu, X. Ruan, E. Pop, *J. Appl. Phys.* **2018**, *123*, 115107.
- [175] Z. Xu, M. J. Buehler, *J. Phys.: Condens. Matter* **2012**, *24*, 475305.



- [176] H. Wang, J. Gong, Y. Pei, Z. Xu, *ACS Appl. Mater. Interfaces* **2013**, 5, 2599.
- [177] C. J. Foss, Z. Aksamija, *2D Mater.* **2019**, 6, 025019.
- [178] G. C. Correa, C. J. Foss, Z. Aksamija, *Nanotechnology* **2017**, 28, 135402.
- [179] B. N. J. Persson, A. I. Volokitin, H. Ueba, *J. Phys.: Condens. Matter* **2011**, 23, 045009.
- [180] B. N. J. Persson, H. Ueba, *J. Phys.: Condens. Matter* **2010**, 22, 462201.
- [181] G. A. Slack, R. G. Ross, *J. Phys. C: Solid State Phys.* **1985**, 18, 3957.
- [182] W.-P. Hsieh, B. Chen, J. Li, P. Keblinski, D. G. Cahill, *Phys. Rev. B* **2009**, 80, 180302.
- [183] B. Chen, W.-P. Hsieh, D. G. Cahill, D. R. Trinkle, J. Li, *Phys. Rev. B* **2011**, 83, 132301.
- [184] A. Giri, J. T. Gaskins, L. Li, Y.-S. Wang, O. V. Prezhdo, P. E. Hopkins, *Phys. Rev. B* **2019**, 99, 165139.
- [185] S. Deng, L. Li, Y. Zhang, *ACS Appl. Nano Mater.* **2018**, 1, 1932.
- [186] H. Yang, X. Yao, L. Yuan, L. Gong, Y. Liu, *Nanoscale* **2019**, 11, 578.
- [187] W.-P. Hsieh, A. S. Lyons, E. Pop, P. Keblinski, D. G. Cahill, *Phys. Rev. B* **2011**, 84, 184107.
- [188] P. Giannozzi, S. Baroni, N. Bonini, M. Calandra, R. Car, C. Cavazzoni, D. Ceresoli, G. L. Chiarotti, M. Cococcioni, I. Dabo, A. D. Corso, S. de Gironcoli, S. Fabris, G. Fratesi, R. Gebauer, U. Gerstmann, C. Gougoussis, A. Kokalj, M. Lazzeri, L. Martin-Samos, N. Marzari, F. Mauri, R. Mazzarello, S. Paolini, A. Pasquarello, L. Paulatto, C. Sbraccia, S. Scandolo, G. Sclauzero, A. P. Seitsonen, A. Smogunov, P. Umari, R. M. Wentzcovitch, *J. Phys.: Condens. Matter* **2009**, 21, 395502.
- [189] S. I. Anisimov, B. L. Kapeliovich, T. L. Perelman, *Sov. Phys. J. Exp. Theor. Phys.* **1974**, 39, 375.
- [190] J. Hohlfeld, S.-S. Wellershoff, J. Güdde, U. Conrad, V. Jähnke, E. Matthias, *Chem. Phys.* **2000**, 251, 237.
- [191] J. M. Ziman, *Electrons and Phonons*, Clarendon Press, Oxford **1960**.
- [192] A. Majumdar, P. Reddy, *Appl. Phys. Lett.* **2004**, 84, 4768.
- [193] J. Lombard, F. Detcheverry, S. Merabia, *J. Phys.: Condens. Matter* **2014**, 27, 015007.
- [194] Z. Li, S. Tan, E. Bozorg-Grayeli, T. Kodama, M. Asheghi, G. Delgado, M. Panzer, A. Pokrovsky, D. Wack, K. E. Goodson, *Nano Lett.* **2012**, 12, 3121.
- [195] M. L. Huberman, A. W. Overhauser, *Phys. Rev. B* **1994**, 50, 2865.
- [196] A. Sergeev, *Phys. B* **1999**, 263–264, 217.
- [197] A. V. Sergeev, *Phys. Rev. B* **1998**, 58, R10199.
- [198] G. D. Mahan, *Phys. Rev. B* **2009**, 79, 075408.
- [199] M. Kaganov, I. Lifshitz, L. V. Tanatarov, *Sov. Phys. J. Exp. Theor. Phys.* **1957**, 4, 173.
- [200] P. B. Allen, *Phys. Rev. Lett.* **1987**, 59, 1460.
- [201] R. H. M. Groeneveld, R. Sprik, A. Lagendijk, *Phys. Rev. B* **1992**, 45, 5079.
- [202] A. Giri, J. T. Gaskins, B. M. Foley, R. Cheaito, P. E. Hopkins, *J. Appl. Phys.* **2015**, 117, 044305.
- [203] X. Wu, T. Luo, *EPL* **2015**, 110, 67004.
- [204] P. E. Hopkins, J. L. Kassebaum, P. M. Norris, *J. Appl. Phys.* **2009**, 105, 023710.
- [205] L. Guo, S. L. Hodson, T. S. Fisher, X. Xu, *J. Heat Transfer* **2012**, 134, 042402.
- [206] P. E. Hopkins, P. M. Norris, *Appl. Surf. Sci.* **2017**, 253, 6289.
- [207] S. Y. Savrasov, D. Y. Savrasov, *Phys. Rev. B* **1996**, 54, 16487.
- [208] R. Bauer, A. Schmid, P. Pavone, D. Strauch, *Phys. Rev. B* **1998**, 57, 11276.
- [209] Y. Wang, X. Ruan, A. K. Roy, *Phys. Rev. B* **2012**, 85, 205311.
- [210] B. Krenzer, A. Hanisch-Blicharski, P. Schneider, T. Payer, S. Möllenbeck, O. Osmani, M. Kammiller, R. Meyer, M. Horn-von Hoegen, *Phys. Rev. B* **2009**, 80, 024307.